

Structural, Dielectric and Ferroelectric Properties of Cu^{2+} and $\text{Cu}^{2+}/\text{Bi}^{3+}$ doped BCZT Lead-free Ceramics: A Comparative Study

Sapna Kumari

Institute for Integrated & Honors Studies: Kurukshetra University, Kurukshetra

Amit Kumar

Institute of Integrated & Honors Studies: Kurukshetra University, Kurukshetra

V. Kumar (✉ vijay.phy19@kuk.ac.in)

Kurukshetra University <https://orcid.org/0000-0002-4560-7581>

S. K. Dubey

Institute of Integrated & Honors Studies: Kurukshetra University, Kurukshetra

P. K. Goyal

Department of Physics, J.C. Bose University of Science & Technology, YMCA, Faridabad, India

Suresh Kumar

Department of Electronics Science: Kurukshetra University, Kurukshetra

A. L. Sharma

Department of Physics: Central University of Punjab, Bathinda

Anil Arya

Department of Physics: Central University of Punjab, Bathinda

Research Article

Keywords: Lead-free ceramics, BCZT, Perovskite, Ferroelectrics, Dielectrics

Posted Date: March 18th, 2021

DOI: <https://doi.org/10.21203/rs.3.rs-314196/v1>

License: © ⓘ This work is licensed under a Creative Commons Attribution 4.0 International License.

[Read Full License](#)

Structural, dielectric and ferroelectric properties of Cu²⁺ and Cu²⁺/Bi³⁺ doped BCZT lead-free ceramics: A comparative study

Sapna Kumari^{1,2}, Amit Kumar^{1,2}, V. Kumar^{1,*}, S. K. Dubey³, P. K. Goyal⁴, Suresh Kumar⁵, A. L. Sharma⁶, and Anil Arya⁶

¹*Department of Physics, Institute of Integrated and Honors Studies (IIHS), Kurukshetra University, Kurukshetra- 136119, India*

²*Department of Physics, Kurukshetra University, Kurukshetra- 136119, India*

³*Department of Chemistry, Institute of Integrated and Honors Studies (IIHS), Kurukshetra University, Kurukshetra- 136119, India*

⁴*Department of Physics, J.C Bose University of Science & Technology, YMCA, Faridabad-121006, India*

⁵*Department of Electronic Science, Kurukshetra University, Kurukshetra- 136119, India*

⁶*Department of Physics, Central University of Punjab, Bathinda-151401, India*

^{*} Corresponding author: vijphykaushik@gmail.com

Abstract Perovskite type Ba_{0.98}Ca_{0.02}Zr_{0.02}Ti_{0.98}O₃ (BCZT), Ba_{0.98}Ca_{0.02}Zr_{0.02}Ti_{0.976}Cu_{0.008}O₃ (BCZTC) and Ba_{0.9725}Bi_{0.005}Ca_{0.02}Zr_{0.02}Ti_{0.976}Cu_{0.008}O₃ (BCZTCB) lead-free ceramics were synthesised via solid-state reaction method at a sintering temperature of ~1380 °C. Effects of CuO and Bi₂O₃/CuO doping on structural, microstructural, dielectric, and ferroelectric properties were investigated systematically. X-ray diffraction technique confirmed the existence of pure perovskite phase with the tetragonal structure in pure and in the doped BCZT ceramics at room temperature. The dielectric analysis demonstrated two anomalies around 24 °C and 126 °C for BCZT, which were identified as orthorhombic to tetragonal (T_{O-T}) and tetragonal to cubic (T_C) phase transition temperature, respectively. The T_{O-T} temperature shifted to below 16 °C, while the T_C increased to 132 °C for the BCZTCB sample. The physical mechanisms of the conduction processes were investigated through impedance spectroscopy and the values of resistance, conductivity, and activation energies associated with the grain and grain boundaries were evaluated. The activation energy was determined to be higher for doped samples than for pure BCZT. Further, the dopant-dependent ferroelectric nature of the ceramic samples was evidenced by the analysis of characteristic hysteresis loop, and a value of remnant polarisation (P_r = 4.59 μC/cm²) was obtained for the BCZTCB ceramic sample. Furthermore, the d₃₃ value, which was 54 pC/N for pure BCZT, was determined to be 140 pC/N and 64 pC/N for BCZTC and BCZTCB, respectively.

Keywords: Lead-free ceramics, BCZT, Perovskite, Ferroelectrics, Dielectrics

1 Introduction

For several decades, the lead-containing perovskite ferroelectric ceramics like $\text{Pb}(\text{Zr,Ti})\text{O}_3$ (PZT) have attracted the attention of the scientific community due to their extraordinary ferroelectric and piezoelectric properties [1–10]. The broad range of applications of these ceramics in sensors, actuators, and other ferroelectric and memory devices, signifies the potential of these materials [9–13]. However, the main hindrance with the use of these materials is the presence of lead (more than 60 wt. %) being toxic, affects human health and the environment [5–9]. Therefore, researchers and scientists are continuously making efforts to develop high-performance lead-free or with negligible lead content ferroelectric ceramics, which can be safely and efficiently used in different scientific and technological applications [9–13].

For this purpose, the intensive studies were performed worldwide to enhance the properties of lead-free ceramics by using suitable dopants, different synthesis route such as solid-state reaction, sol-gel & hydrothermal methods and by optimizing the synthesis parameters [13-64]. Among all lead-free ferroelectric ceramics with perovskite structure such as $(\text{Bi}_{0.5}\text{Na}_{0.5})\text{TiO}_3$ (BNT), BaTiO_3 (BT) and $(\text{K,Na})\text{NbO}_3$ (KNN) based systems; BT-based system (especially - $\text{Ba}_{0.85}\text{Ca}_{0.15}\text{Zr}_{0.1}\text{Ti}_{0.9}\text{O}_3$) has gained more attention because of its high piezoelectric coefficient comparable to PZT (~ 660 pc/N) [7]. However, the low Curie temperature ($T_C \sim 90$ °C) restricts its use at a higher temperature. Further, high sintering temperature (≥ 1500 °C) causes energy consumption and fabrication cost issues [8, 9]. However, some studies indicate that by changing the stoichiometry composition from $\text{Ba}_{0.85}\text{Ca}_{0.15}\text{Zr}_{0.1}\text{Ti}_{0.9}\text{O}_3$ to $\text{Ba}_{0.98}\text{Ca}_{0.02}\text{Ti}_{0.98}\text{Zr}_{0.02}\text{O}_3$ or $\text{Ba}_{0.99}\text{Ca}_{0.01}\text{Zr}_{0.02}\text{Ti}_{0.98}\text{O}_3$, Curie temperature can be increased up to 120 °C [22-25, 27-29, 64-65], but there is still a problem of high sintering temperature (≥ 1500).

Therefore, more attention has been given to synthesise the BT based BCZT ceramic system with enhanced T_C temperature, improved ferroelectric and piezoelectric properties at a sintering temperature as low as possible [10, 11, 13, 14]. Doping of oxides such as CuO, MnO_2 , Bi_2O_3 , and ZnO as a sintering aid is a better strategy to improve the dense microstructure and to decrease the sintering temperature of BCZT ceramics [15–28]. Because of the low melting point of CuO (1026 °C) and Bi_2O_3 (825 °C), liquid formation occurs below the sintering temperature, which facilitates the densification process and improves the electric properties [20, 24].

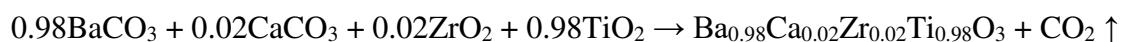
In literature, the introduction of Cu in BCZT was also reported to shift the orthorhombic

to tetragonal (T_{O-T}) phase transition towards lower temperature, while maintaining the Curie temperature (T_C) [17, 18, 24]. $Ba_{0.98}Ca_{0.02}Zr_{0.02}Ti_{0.98}O_3$ -0.8 mole% Cu lead-free ceramic, synthesized at a lower sintering temperature (1250 °C), was reported to have enhanced temperature stability range and good electrical properties [24]. The substitution of Bi_2O_3 was also reported to decrease the sintering temperature and to increase the Curie temperature [25]. Improvement in the Curie temperature of $BaTiO_3$ was attained through Cu^{2+}/Bi^{3+} substitution as reported by N. Kumada *et al.* [26]. X. Wang *et al.* reported a diffuse phase transition with a slight decrease in T_C for Cu^{2+}/Bi^{3+} modified $Ba_{0.85}Ca_{0.15}Zr_{0.1}Ti_{0.9}O_3$ [20]. Similarly, $Ba_{0.98}Ca_{0.02}Zr_{0.02}Ti_{0.98}O_3$ ceramics, modified by different dopants were reported with better dielectric, ferroelectric and piezoelectric properties [13, 24, 27, 28]. However, the effects of simultaneous addition of Cu^{2+} and Bi^{3+} on structural, dielectric, and ferroelectric properties of $Ba_{0.98}Ca_{0.02}Zr_{0.02}Ti_{0.98}O_3$ ceramics are rarely reported.

In the present work, we synthesised pure, Cu^{2+} and Cu^{2+}/Bi^{3+} modified $Ba_{0.98}Ca_{0.02}Zr_{0.02}Ti_{0.98}O_3$ ceramics via a solid-state reaction method at a sintering temperature of ~1380 °C and investigated the structural, dielectric, and ferroelectric properties. Here we demonstrated that simultaneous doping of Cu^{2+}/Bi^{3+} led to significant improvement in the Curie temperature and temperature stability range for dielectric properties.

2 Experimental procedure

$Ba_{0.98}Ca_{0.02}Zr_{0.02}Ti_{0.98}O_3$ (BCZT), $Ba_{0.98}Ca_{0.02}Zr_{0.02}Ti_{0.976}Cu_{0.008}O_3$ (BCZTC) and $Ba_{0.9725}Bi_{0.005}Ca_{0.02}Zr_{0.02}Ti_{0.976}Cu_{0.008}O_3$ (BCZTCB) were synthesised via solid-state reaction method (Fig. 1). The raw materials $BaCO_3$ (99 %), $CaCO_3$ (99 %), TiO_2 (99.9 %), ZrO_2 (99 %), Bi_2O_3 (99 %) and CuO (99 %) were dehydrated at 180 °C for 2 h. To get a homogenous mixture, the dehydrated raw materials were ground in an agate mortar and pastel for 5 h and then calcined at 1200 °C for 3 h. After mixing thoroughly with a 6 wt. % polyvinyl alcohol (PVA) binder solution, the resulting mixture was pressed into disk samples with ~10 mm diameter and ~1 mm thickness. After burning out PVA, pellets were sintered at 1380 °C for 3 h at the heating rate of 5 °C/min. The reaction equation for pure BCZT is as follows.



Further, for electrical measurements, sintered pellets were coated with silver paste on both sides and fired at 250 °C for 1 h to make conductive electrodes.

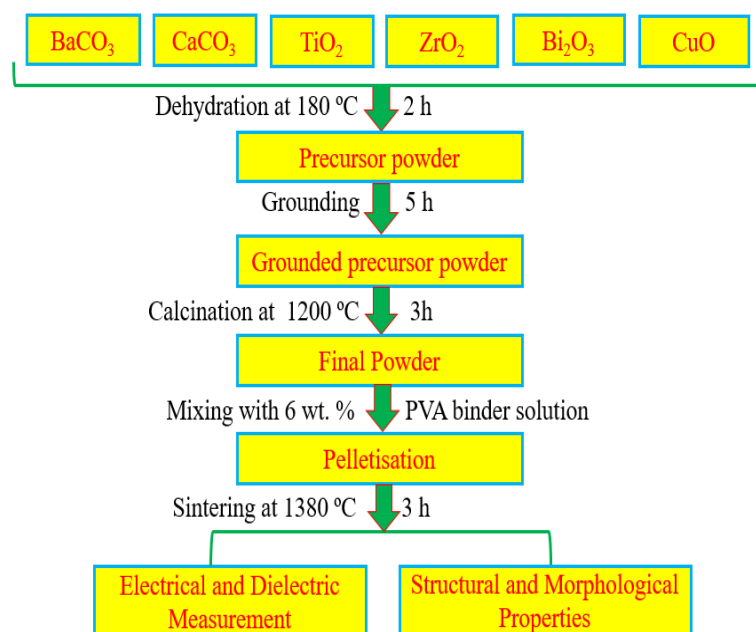


Fig. 1 The schematic diagram showing the different steps of solid-state reaction method followed for the synthesis of BCZT based ceramic samples.

The phase structure was characterized by X-ray diffraction (XRD) technique (Rigaku Ultima-IV, Germany) using Cu-K α radiation in Bragg's angle ranging from 20° to 80° with a step size of 0.02°. After confirming the phase formation, structural analysis was probed by the Rietveld refinement method using FULLPROF software, which is a well-established technique to evaluate the structural parameters. Scanning Electron Microscope (SEM) (JEOL JSM-6390LV) equipped with Energy Dispersive X-ray microscopy (EDX) was used for the microstructural and elemental compositional analysis. The bulk density of the sintered pellets was determined by the Archimedes method. A precision impedance analyser (Wayne Kerr 6500B) was employed to characterize the dielectric properties at various frequencies. The polarization hysteresis (P–E) loops were measured using a Radiant ferroelectric tester (Model no. 609B) at room temperature at 10 Hz. The sintered pellets were poled at ambient temperature for 40 min in silicon oil before piezoelectric properties measurements. The values of piezoelectric coefficient d_{33} were measured by using the d_{33} meter (Model YE2730).

3 Results and Discussion

3.1 Phase structure analysis

X-ray diffraction patterns (Fig. 2), confirm the presence of pure perovskite phase without any trace of impurity. This indicates that doped ions successfully diffuse into the crystal lattice of host BCZT to form a homogeneous solution [29, 30], while the narrow and intense XRD

peaks indicate good crystallinity of the samples. The appearance of peaks (002) and (200) at around $2\theta = 45^\circ$ (inset of Fig. 2) indicates the tetragonal structure for all samples [25, 30, 31]. Further, a shift of peaks has been observed after doping, which may be either due to ionic size or valency effect. According to the tolerance factor, smaller ions (radii $< 0.87 \text{ \AA}$) will occupy the B-site, larger ions (radii $> 0.94 \text{ \AA}$) occupy A-site while intermediate ions can occupy both sites [24]. From this viewpoint, Cu^{2+} would be substituted at the B-site due to a lower ionic radius (0.73 \AA). If we consider the ionic size effect, lattice expansion should occur due to the large ionic radius of Cu^{2+} compared to Ti^{4+} (0.68 \AA) and Zr^{4+} (0.72 \AA) and should cause a lower angle shift of peaks in XRD. However, contrary to this lower angle shifting, a higher angle shifting of (200) peaks has been observed in XRD patterns. The higher angle shifting of the peaks and the decrease in the value of the unit cell volume in the case of BCZTC compared to BCZT ceramic (Table. 1), indicates the shrinkage of the lattice, which can be attributed to the generated oxygen vacancies due to the lower valence state of Cu^{2+} compared to $\text{Ti}^{4+}/\text{Zr}^{4+}$ [24].

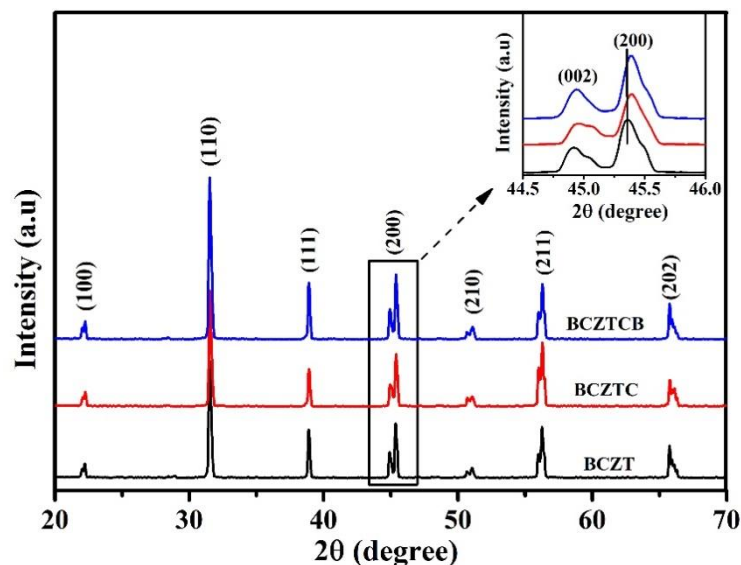


Fig. 2 XRD patterns of sintered BCZT, BCZTC and BCZTCB ceramic samples (inset shows the enlarged region for $2\theta = 44.5^\circ - 46^\circ$).

However, in case of Bi^{3+} substitution in BCZTC, the observed higher angle shifting of peaks (Fig. 2) can be attributed to the fact that Bi^{3+} (1.17 \AA) having a smaller ionic radius compared to Ba^{2+} (1.61 \AA) and Ca^{2+} (1.34 \AA), in accordance with the tolerance factor, substitutes at the A-site [32, 33].

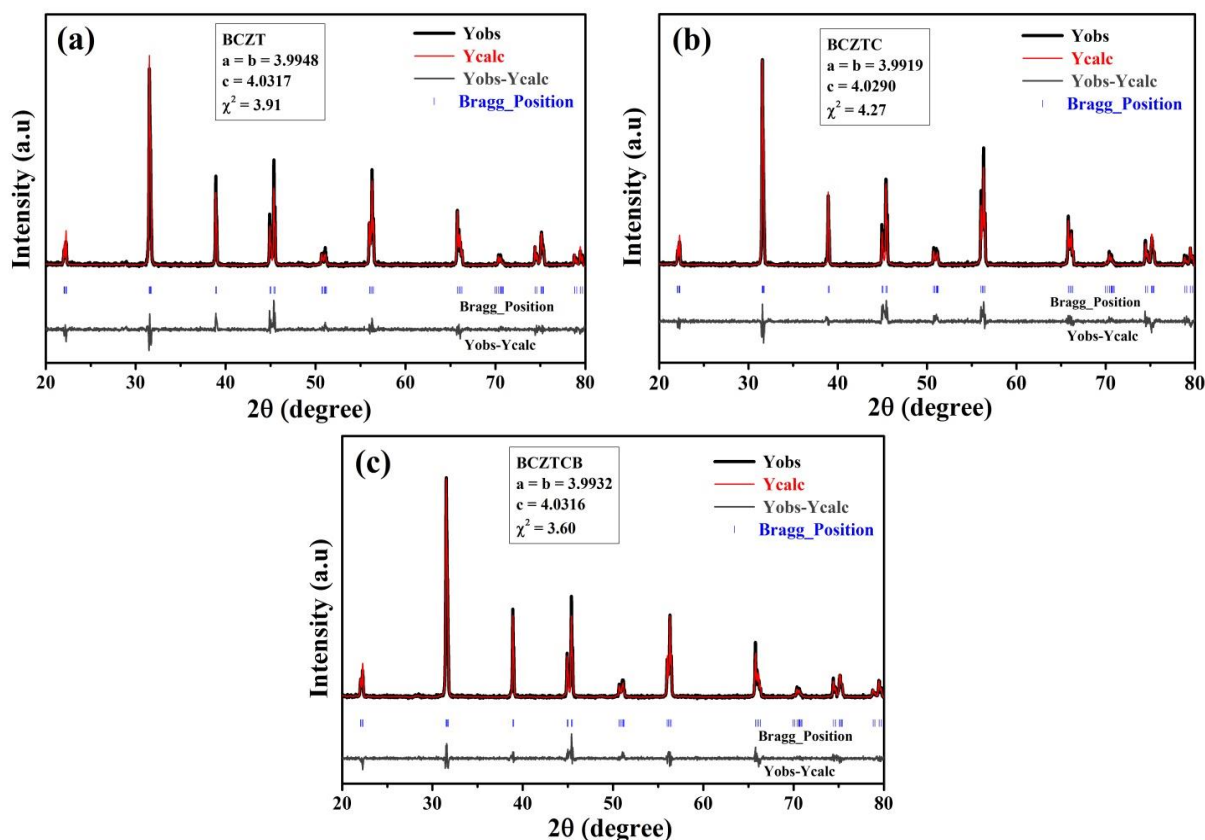


Fig. 3 Rietveld refinement fitting for (a) BCZT, (b) BCZTC and (c) BCZTCB ceramic samples.

Table 1 Rietveld refinement parameters for BCZT, BCZTC and BCZTCB ceramic samples

Parameters	BCZT			BCZTC			BCZTCB		
a=b (Å)	3.9948			3.9919			3.9932		
c (Å)	4.0317			4.0290			4.0316		
$\alpha = \beta = \gamma$	90°			90°			90°		
c/a	1.0092			1.0092			1.0096		
Direct cell volume (Å) ³	64.3407			64.2031			64.2882		
Density (g/cc)	5.991			6.012			6.050		
χ^2	3.91			4.27			3.60		
Atomic Coordinates	x	y	z	x	y	z	x	Y	z
Ba	0	0	-0.26029	0	0	-0.03219	0	0	0.43545
Ca	0	0	-0.26029	0	0	-0.03219	0	0	0.43545
Zr	1/2	1/2	0.27764	1/2	1/2	0.42942	1/2	1/2	0.93178
Ti	1/2	1/2	0.27764	1/2	1/2	0.42942	1/2	1/2	0.93178
O(1)	1/2	1/2	-0.22545	1/2	1/2	-0.07182	1/2	1/2	0.39558
O(2)	1/2	0	0.25963	1/2	0	0.56385	1/2	0	0.96209
Cu	-	-	-	1/2	1/2	0.42942	1/2	1/2	0.93178
Bi	-	-	-	-	-	-	0	0	0.43545
Space group	P 4 m m			P 4 m m			P 4 m m		
Crystallite size (nm)	37.90			40.24			36.81		
Exp. density (g/cc)	5.40			5.42			5.57		
Grain size (μm)	19.73			16.14			10.81		

To find the precise value of the lattice parameters and to confirm the crystal structure, XRD spectra of all samples are further analysed by Rietveld refinement using the Fullprof software (Fig. 3) [37]. The refinement is done using the pseudo-Voigt profile function. In the first step, the global parameters (background and scale factors) are refined. In the next step, the structural parameters such as cell parameters, profile shape, asymmetry parameters, preferred orientation, atomic positions, and site occupancies are refined sequentially. The fitting quality of the experimental data has been evaluated by computing the parameters such as the “goodness of fit” χ^2 and the R-factors [38]. The solid red line is the best fit to the scattered data (Fig. 3), the vertical lines represent the Bragg positions for the space group, and the lower curve shows the difference between the observed and the calculated profiles. The refined XRD patterns indicate that the samples have a tetragonal structure with the P4mm space group. The values of refinement parameters such as χ^2 , lattice constant parameters, direct cell volume, atomic coordinates, and space group for all the ceramic samples are listed in Table 1. The crystallite size has been calculated by taking the data corresponding to the maximum intensity diffraction peak [110] by Scherrer’s equation (Eq. 1) [35-36].

$$D = \frac{K*\lambda}{\beta* \cos\theta} \quad (1)$$

Where, K = Scherrer’s constant (0.9), λ = wavelength of X-ray (1.54 Å), β = full width at half maxima (FWHM), θ = Bragg’s diffraction angle, D = crystallite size.

Further, we ascertain that density of BCZT ceramic increases after Cu^{2+} and simultaneous $\text{Cu}^{2+}/\text{Bi}^{3+}$ addition (Table 1), which may be credited to the liquid phase sintering. During the sintering process, the liquid formation occurs due to the low melting point of CuO (1026 °C) and Bi_2O_3 (825 °C) in comparison to sintering temperature, which pulls the grains to come closer by providing capillary force [20-21, 24, 34].

3.2 Microstructural analysis

Figure 4 (a-c) demonstrates the SEM micrograph and corresponding EDX spectra of pure BCZT, BCZTC, and BCZTCB ceramics, respectively. Analysis of Fig. 4(a) shows the non-uniform grain size distribution, which indicates the anisotropic process of grain growth in pure BCZT. The Cu^{2+} addition has relatively improved the uniformity of grains for BCZTC and exhibit distinct grain boundaries with an increase in porosity compared to pure BCZT. However, a denser microstructure with increased anisotropy in grain size has been observed for BCZTCB (Fig. 4c). Further, the average grain size calculated using ImageJ software has

decreased from 19.73 μm (BCZT) to 10.81 μm (BCZTCB) (Table 1), which shows that $\text{Cu}^{2+}/\text{Bi}^{3+}$ acts as a grain growth inhibitor. Similar observations were also reported in literature for Bi modified $\text{Ba}(\text{Zr},\text{Ti})\text{O}_3$ and $\text{Bi}_2\text{O}_3/\text{CuO}$ doped $\text{Ba}_{0.85}\text{Ca}_{0.15}\text{Zr}_{0.1}\text{Ti}_{0.9}\text{O}_3$ [20, 32]. The observed decrease in grain size can be correlated with the accumulation of additives around grain boundaries when the content of doping was beyond their solubility limit in the host matrix (BCZT) and inhibit the growth of grains [22, 24, 34, 39]. The small grain size also suggests that the present ceramic has a high dielectric breakdown strength, and is desirable [40]. Thus, it can be concluded that a small amount of copper and bismuth can affect the surface morphology and grain size of BCZT ceramics.

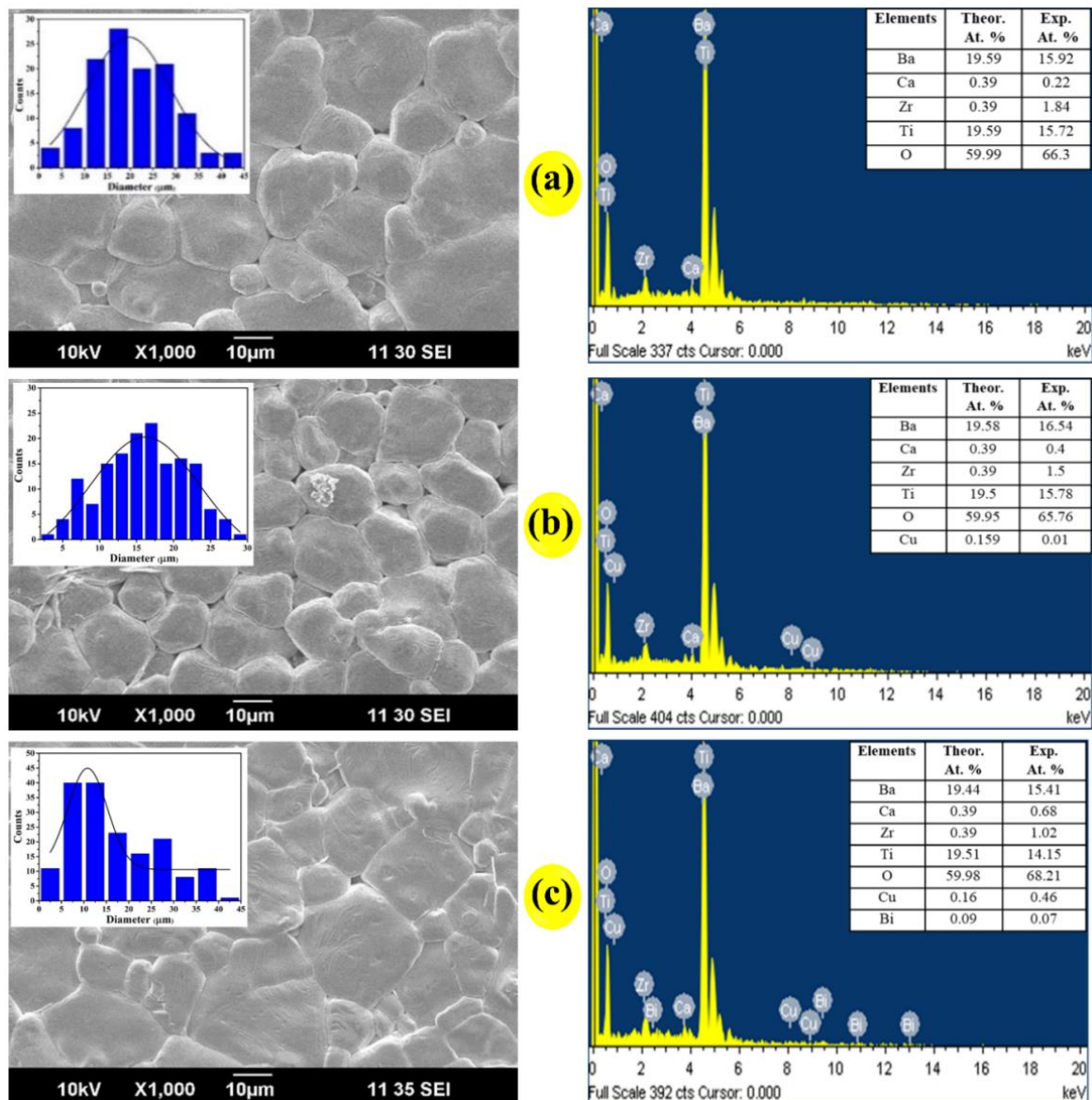


Fig. 4 SEM images and EDX spectra of (a) BCZT (b) BCZTC (c) BCZTCB ceramic samples (Inset: grain size distribution and Comparison of atomic % detected by EDX).

To ascertain the elemental distribution, Energy Dispersive X-Ray (EDX) technique was performed and the corresponding distribution of elements is shown in Fig. 4. The EDX analysis reveals the presence of all elements in an appropriate amount in arbitrarily selected regions and no impurity elements have been detected. A deviation in the theoretical and experimental elemental compositions has been observed (given in the inset tables in EDX spectra), which may be attributed either due to the adopted synthesis process or to the accuracy of the EDX technique [41].

3.3 Temperature-dependent dielectric analysis

Figure 5(a) depicts the variation of dielectric properties (dielectric permittivity- ϵ_r and dielectric loss-tan δ) with the temperature at 1 kHz. Two dielectric anomalies corresponding to the orthorhombic-tetragonal (T_{O-T}) and tetragonal to cubic (T_C) phase transitions have been observed at 24 °C and 126 °C, respectively, for BCZT ceramic sample [18]. The presence of the tetragonal phase at room temperature is also supported by the analysis of XRD spectra (Fig. 2). After the introduction of copper into BCZT, the T_{O-T} transition shifts to a slightly lower temperature (22 °C), while no effect has been detected on T_C [24]. However, simultaneous doping of Cu^{2+} and Bi^{3+} strongly improves the temperature stability range by shifting the T_{O-T} further to lower temperature even below the starting temperature of the studied range (*i.e.* 16 °C) and T_C at a higher temperature (132 °C) in comparison of pure BCZT, which makes it a promising candidate for electrical devices [42]. Such an improvement in the Curie temperature may be correlated with the small grains as the inner stress is large in small grains and reduces the space-charge field strength [43].

These phase transition temperatures (T_{O-T} & T_C) for BCZTC & BCZTCB ceramics are significantly improved compared to other CuO and Bi_2O_3 modified $Ba_{0.98}Ca_{0.02}Zr_{0.02}Ti_{0.98}O_3$ ceramics reported in literature [13, 20, 27]. Further studies are in progress to investigate the dependence of T_C and other properties on different combinations of Cu^{2+} and Bi^{3+} doping in $Ba_{0.98}Ca_{0.02}Zr_{0.02}Ti_{0.98}O_3$ ceramics.

The values of dielectric permittivity (ϵ_r) plotted in Fig. 5, were calculated by using the following formula [44]:

$$\epsilon_r = \frac{(C * d)}{(A * \epsilon_0)} \quad (2)$$

Where $\epsilon_0 = 0.0885$ pF/cm is the permittivity in vacuum, C is the capacitance of the specimen, d is the sample thickness and A is the cross-sectional area of the specimen in cm^2 .

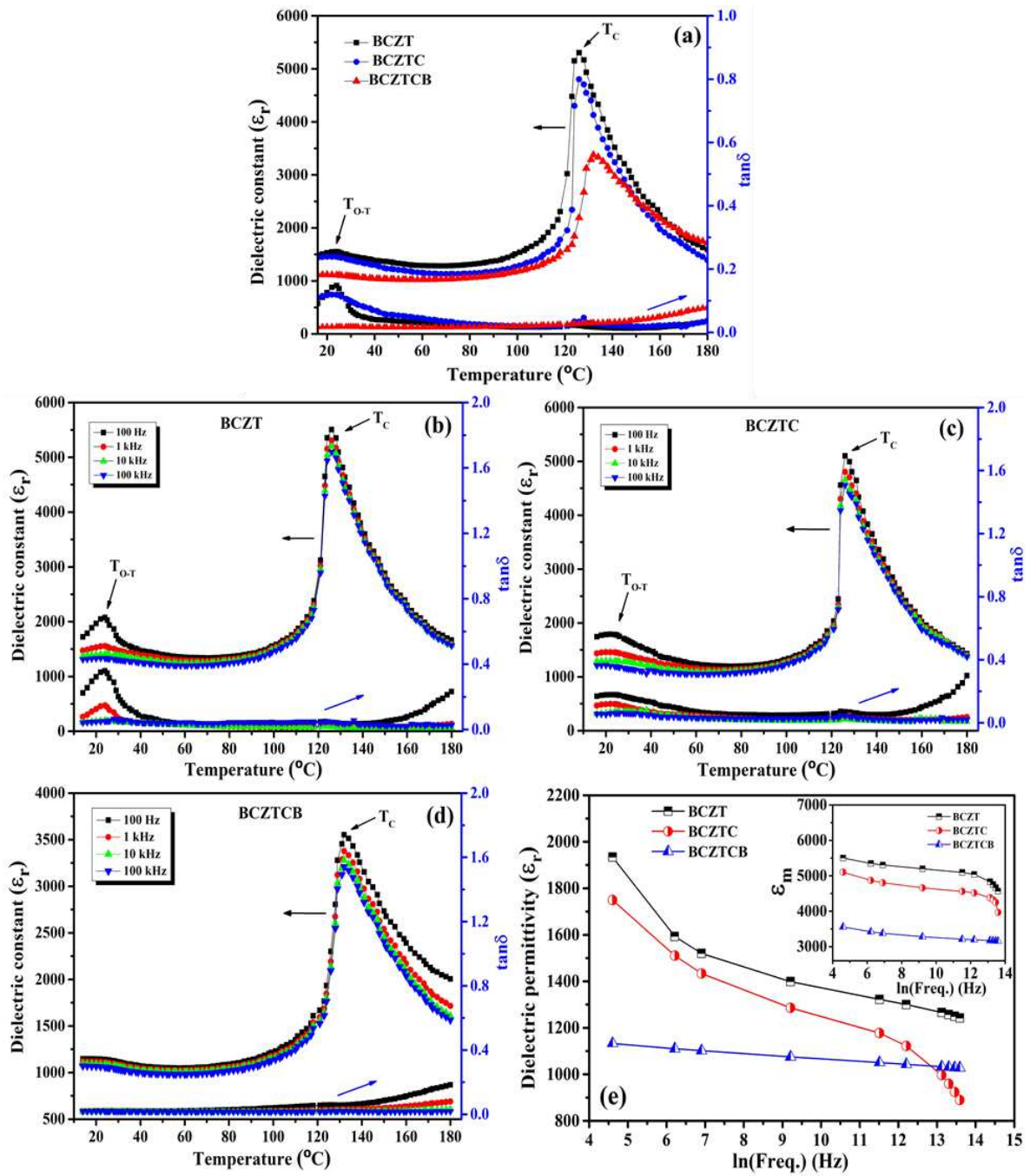


Fig. 5 Temperature dependence of dielectric permittivity and loss (a) at 1 kHz, (b-d) at different frequencies (e) frequency dependence of room temperature dielectric permittivity (Inset shows maximum dielectric permittivity vs. frequency).

All the samples show high value of dielectric permittivity (ϵ_{\max} and ϵ_r -at room temperature) and a low value of dielectric loss ($\tan\delta$), with a decreasing trend in the dielectric permittivity (ϵ_r) and increment in dielectric loss (Fig. 5(a) & Table 2) after doping of Cu^{2+} and simultaneous doping of $\text{Cu}^{2+}/\text{Bi}^{3+}$ in BCZT ceramic. The decrease in permittivity may be due to the difficulty of the polarisation reversal process of domains in small grains [24, 45]. Such types of results for phase transition temperatures and dielectric permittivity for Cu^{2+} and Bi^{3+} modified BT based ceramics have also been reported in the literature [21, 22, 24–26,

46]. BCZTCB shows more temperature stability for dielectric properties in comparison to BCZT and BCZTC which makes it suitable for a high dielectric constant capacitor within a long temperature range [47].

Further analysis of the plots of variation of dielectric permittivity with temperature measured at different frequencies (Fig. 5 (b - d)), demonstrates that the Curie temperature (T_C) is independent of frequency variations for all samples. It is also worth noting from Fig. 5 (e) that the dielectric permittivity at room temperature as well as at T_C (ϵ_r and ϵ_{max} respectively) shows a weak dependence on frequency variation for BCZT sample simultaneously doped with Cu^{2+} & Bi^{3+} .

Table 2 Dielectric properties of synthesized samples measured at 1 kHz

Samples	T_C (°C)	T_{O-T} (°C)	ϵ_{max}	$\tan \delta$ (At T_C)	T_{cw} (°C)	ϵ_r (at RT)	γ	ΔT_m (°C)
BCZT	126	24	5305	0.021	114	1520	1.25	21
BCZTC	126	22	4803	0.034	116	1434	1.35	31
BCZTCB	132	< 16	3377	0.030	91	1102	1.29	14

Above Curie temperature, Dielectric permittivity follows the Curie Weiss law [48] as given below,

$$\epsilon_r = \frac{C}{T - T_{cw}} \quad (3)$$

Where C is the curie Weiss constant and T_{cw} is the Curie Weiss temperature. Plots of the reciprocal of dielectric permittivity versus temperature demonstrate the deviation of ϵ_r from the Curie Weiss law as shown in Fig. 6.

To evaluate the phase transition behaviour, modified Curie Weiss law was used [48],

$$\frac{1}{\epsilon} - \frac{1}{\epsilon_m} = \frac{(T - T_m)^\gamma}{C} \quad (1 < \gamma < 2) \quad (4)$$

Where C is the Curie-Weiss constant, ϵ_m is the maximum permittivity, T_m ($= T_C$) is the temperature corresponding to maximum permittivity. The value of γ provides information about the degree of diffuseness, and it ranges from 1 (normal ferroelectrics, Curie-Weiss law) to 2 (ideal relaxor ferroelectrics, Smolenskii–Isupov law), while the materials with the value from 1 to 2 show diffuse characteristics [12, 35].

The values of γ have been determined from the plot of $\ln(1/\epsilon - 1/\epsilon_m)$ vs. $\ln(T - T_m)$ (insets in Fig. 6) and are presented in Table 2. The values of γ reveal that ceramic samples prepared either with Cu^{2+} or Cu^{2+}/Bi^{3+} have diffuse phase transition behaviour.

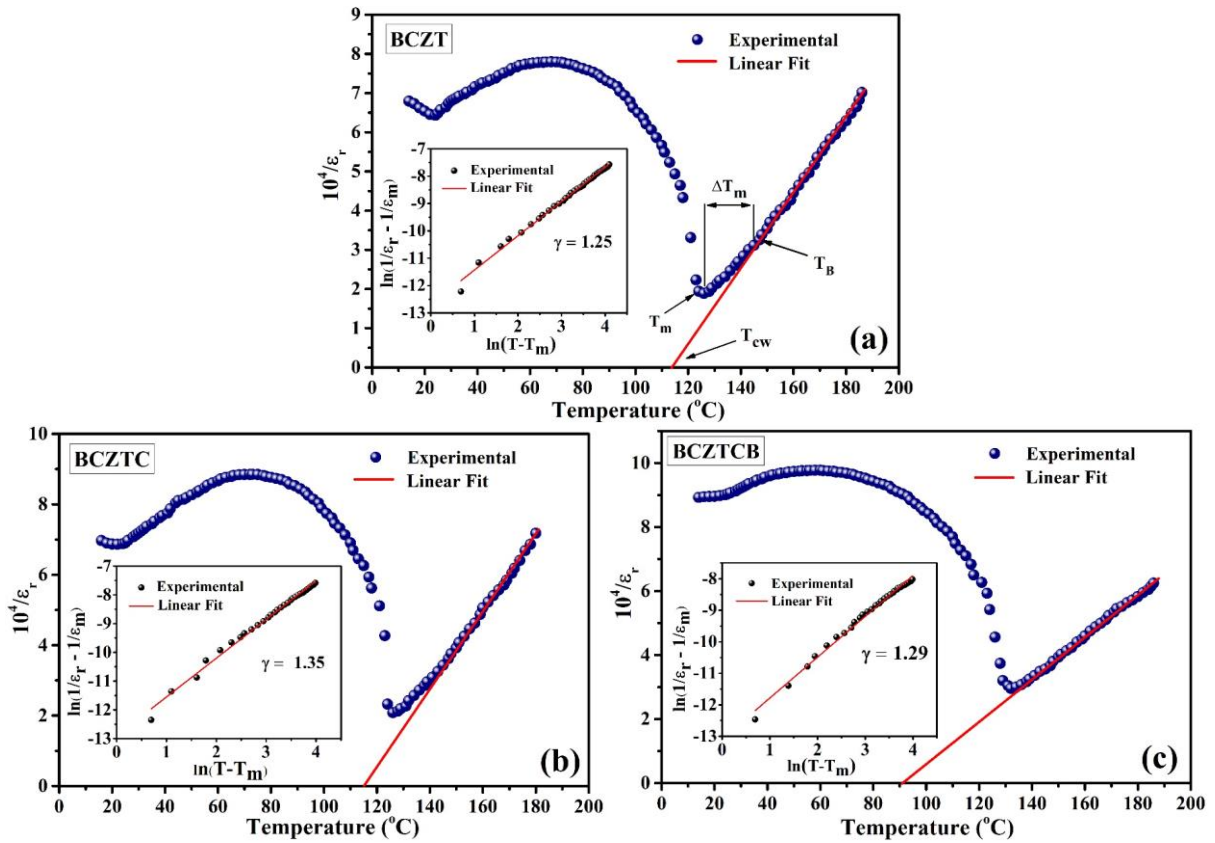


Fig. 6 Temperature dependence of inverse dielectric constant (a) BCZT, (b) BCZTC, (c) BCZTCB and Insets; Plot of $\ln(1/\epsilon - 1/\epsilon_m)$ vs. $\ln(T-T_m)$ at 1 kHz.

To understand the contribution of grains and grain boundaries in the impedance and correlated properties of prepared ceramics, we have measured electrical properties via the impedance spectroscopy. Ceramics consists of randomly oriented grains (g) that are joined together and this joining region is called grain boundaries (gb). This technique gives the measurement of electrical impedance, which is a combination of resistance and reactance as a function of frequency [49]. The Impedance is given by $Z = Z' - j Z''$; where Z' and Z'' are the real and imaginary parts of the complex impedance Z . The impedance data Z and θ were taken from the impedance analyser and then the values of Z' and Z'' were calculated as $Z' = Z \cos\theta$, $Z'' = Z \sin\theta$ [50].

Fig. 7 shows the variation of the real part (Z') and imaginary part (Z'') of impedance (Nyquist plots) of the prepared ceramic samples measured at 350 °C, 400 °C, 450 °C and 500 °C as a function of frequency in the range 100 Hz to 1 MHz. The presence of two semicircles in the spectra confirms that both grain and grain boundaries contribute to the conduction mechanism (Fig. 7 a-c). The high-frequency semi-circle is attributed to the contribution of the grain while the low-frequency semi-circle is associated with the grain boundary. All the impedance plots have been simulated with an electrical equivalent circuit by Z_{SimpWin} software (Fig. 7). The equivalent circuit consists of a parallel combination of resistance (R_g)

and constant phase element (CPE1) in series with another parallel combination of resistance (R_{gb}) and constant phase element (CPE2). The presence of two semi-circles is a signature of electrically heterogeneous behaviour of ceramic samples in the measured range of temperature [20]. The Inset in Fig. 7 a-c shows the Nyquist plot at 350 °C, 400 °C, and solid line is the fitted plot.

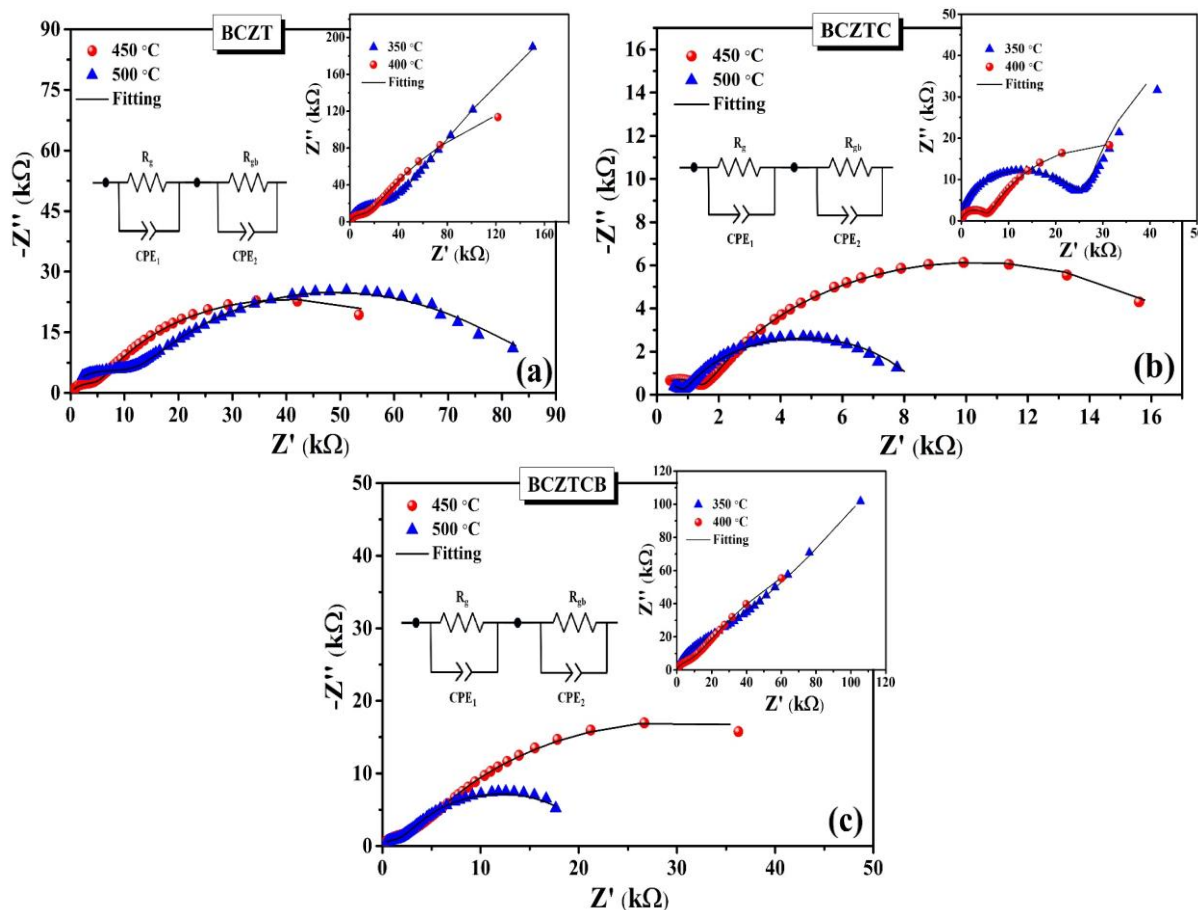


Fig. 7 Nyquist plots of (a) BCZT, (b) BCZTC and (c) BCZTCB ceramics at temperatures (450 °C & 500 °C). Insets: Nyquist plots of (a) BCZT, (b) BCZTC and (c) BCZTCB at temperatures (350 °C & 400 °C).

In the low-frequency region, the radius of the semicircles decreases with the increase in temperature, which characterises the negative temperature coefficient of resistance (NTCR) type behaviour of the samples [20, 51-53]. Such type of behaviour can be attributed to the decrease in grain and grain boundary resistances with increasing temperature (Table 3) as these resistances are related to the diameter of the semicircles. For all samples the grain boundary resistance value is higher compared to grain resistance because the grain boundaries are normally more insulating and capacitive than grains [54]. With the increase in temperature, grain boundary resistance decreases and conductivity increases and can be attributed to the ionisation of oxygen vacancies at high temperatures [55].

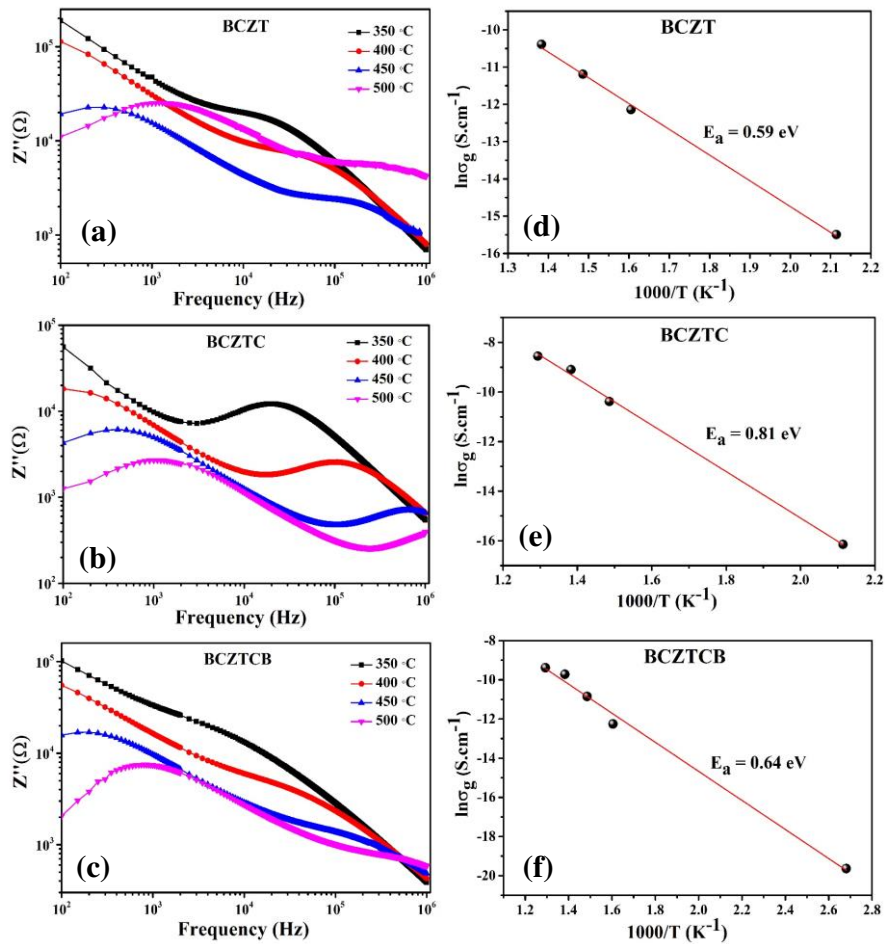


Fig. 8 Frequency dependent imaginary part of impedance at different temperatures, (a) BCZT, (b) BCZTC, and (c) BCZCB. (d-f) plots of $\ln(\sigma_g)$ vs $1000/T$ for BCZT, BCZTC, and BCZCB respectively.

Fig. 8(a-c) displays the variation of the imaginary part (Z'') of impedance with frequency on a log scale at various temperatures. The impedance peaks are shifted towards higher frequencies as the temperature increases, indicating the relaxation behaviour for all samples [51]. Z'' follows a decreasing trend with increase in temperature and frequency, which may be attributed to the rise in conductivity as the temperature and frequency increases [53]. Two peaks that appear at lower and higher frequency regions can be attributed to the relaxation process associated with grain boundary and grains, respectively. The high-frequency peaks become weak for BCZTCB, which is consistent with the Nyquist plot (Z'' vs Z') indicating the decrease in electrical heterogeneity. This may be due to the melting of $\text{CuO}/\text{Bi}_2\text{O}_3$ during the high sintering process and improve the transfer of mass and energy between reactants [20]. The decrease in peak heights with an increase of temperature suggests the close relationship between the impedance relaxation time and the electrical (DC) conductivity.

The values of DC conductivity for the grain and the grain boundaries were calculated from the fitted data obtained from the Nyquist plot and the following formula:

$$\sigma = \frac{t}{R.A} \quad (5)$$

Where, t-thickness of the sample, R- resistance (R_g for grain and R_{gb} for grain boundary) and A is the surface area of the electrode.

Further, it is clear from Table 3 that conductivity increases with the rise in temperature for both grain and grain boundaries. The plots of $\ln(\sigma_g)$ vs $1000/T$ (Fig. 8d-f) are fitted with the Arrhenius equation (Eq. 6);

$$\sigma = \sigma_0 \exp\left(\frac{-E_a}{k_B T}\right) \quad (6)$$

where, σ_0 - pre-exponential factor, k_B - Boltzmann's constant, T- measured temperature and E_a is the activation energy.

The values of activation energy of the relaxation processes in grains have been evaluated from the slope of the fitted line (Fig. 8d-f). The values of the resistance, conductivity, and the activation energies associated with the grain and grain boundaries are listed in Table 3. The value of activation energy has been determined to be higher for doped samples compared to pure BCZT ceramics (Table 3), which indicates the difficult movement of oxygen vacancies.

Table 3 Impedance fitted circuit parameters for BCZT, BCZTC and BCZTCB samples

	T (°C)	R_g (k Ω)	R_{gb} (k Ω)	σ_g (S. m ⁻¹)	σ_{gb} (S. m ⁻¹)	E_g (eV)	E_{gb} (eV)
BCZT	350	29.4	584	0.00053	0.0000268	0.59	0.33
	400	11.4	389	0.00138	0.0000402		
	450	5.1	69	0.00307	0.000228		
	500	9.7	82	0.00161	0.000192		
BCZTC	350	24.4	137	0.00048	0.000086	0.81	2.061
	400	5.1	60	0.00234	0.000198		
	450	1.4	19	0.00848	0.000627		
	500	0.8	8	0.0146	0.00147		
BCZTCB	350	28.3	289	0.00048	0.0000468	0.64	1.332
	400	7.0	185	0.00194	0.0000731		
	450	2.3	62	0.00601	0.000220		
	500	1.6	22	0.00843	0.000613		

3.4 Ferroelectric properties

This section is devoted to the study of the effects of dopants on the ferroelectric properties of BCZT ceramics. Fig. 9(a) depicts the room temperature polarisation-electric field (P-E) hysteresis loops for synthesised samples under a maximum electric field of 20kV/cm at 10 Hz

and the calculated values from P-E loops are summarised in Table 4. The P-E loop exhibits a decrease in remnant polarization (P_r) and coercive field (E_c) for BCZTC ceramic, while an improvement in P_r has been observed for $\text{Cu}^{2+}/\text{Bi}^{3+}$ co-doped BCZT. The ferroelectric properties are highly dependent on size, shape & distribution of grains, the porosity of the material, the generation of oxygen vacancies, etc. [40-46]. As the remnant polarization is also affected by the porosity of the samples and reported to decrease with the increase in porosity [56, 57]. Therefore, the decrease in the value of P_r for BCZTC in comparison of BCZT may be correlated to the presence of more porosity in BCZTC as compared to BCZT ceramic (Fig. 4 a, b). Further, the increase in the value of P_r for BCZTCB ceramic may be attributed to its relatively denser microstructure (Fig. 4c). It should also be noted that these properties can be tailored further by increasing the applied electric field as P-E loop is not completely saturated under 20kV/cm [58].

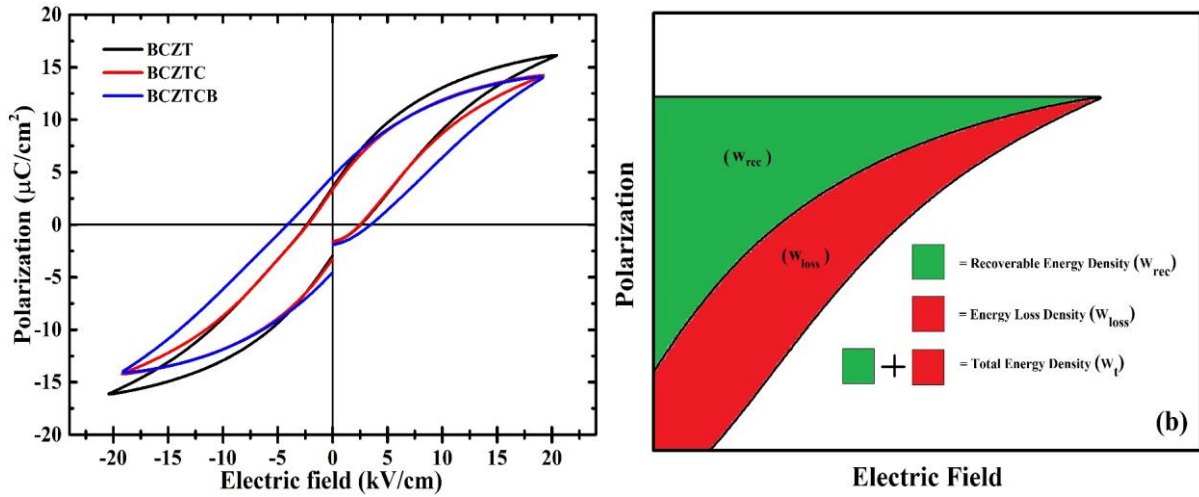


Fig. 9 (a) P-E Hysteresis loop at 10 Hz for BCZT, BCZTC and BCZTCB ceramics **(b)** schematic representation of the areas representing the recoverable energy density, Energy loss density and total energy.

For the investigation of energy storage performance of these BCZT based ceramic samples, the recoverable energy storage density (W_{rec}) and efficiency (η) (listed in Table 4) have been evaluated from the P-E hysteresis loops according to the following relations [59]:

$$W_{rec} = \int_{P_r}^{P_{max}} EdP \quad (7)$$

$$W_t = \int_0^{P_{max}} EdP \quad (8)$$

$$\eta = \frac{W_{rec}}{W_t} \times 100\% \quad (9)$$

Where, W_{rec} , W_t , and η are recoverable energy density, total energy density and energy efficiency (Fig. 9b), while P_{max} , P_r , E and P represent maximum polarization, remnant polarization, electric field and polarization, respectively.

Table 4 The values of various parameters calculated from P-E hysteresis loops

Sample	P_{max} ($\mu\text{C}/\text{cm}^2$)	$+P_r$ ($\mu\text{C}/\text{cm}^2$)	$+E_c$ (kV/cm)	W_{rec} (mJ/cm^3)	W_t (mJ/cm^3)	η (%)
BCZT	16.1	3.58	2.58	82	159	51.5
BCZTC	14.2	3.34	2.49	66	130	50.7
BCZTCB	14.0	4.59	3.47	60	152	39.5

It is clear from Table 4 that the value of efficiency (η) declined from ~51.5 (for BCZT) to ~39.5 (for BCZTCB), which may be due to the relatively high value of P_r and leakage current [60, 61]. Furthermore, the d_{33} value, which is 54 pC/N for pure BCZT, has been determined to be 140 pC/N and 64 pC/N for BCZTC and BCZTCB, respectively.

Table 5 compares the dielectric and ferroelectric properties of our samples with other reported results of BT based ceramics modified by various dopants and synthesized by the solid-state method.

Table 5 A Comparison of the dielectric and ferroelectric properties of lead-free BT based ceramics

Composition	Dopant	Sintering	T_{O-T} ($^{\circ}\text{C}$)	T_C ($^{\circ}\text{C}$)	ϵ_m	ϵ_r	P_{max} ($\mu\text{C}/\text{cm}^2$)	P_r ($\mu\text{C}/\text{cm}^2$)	E_c (kV/cm)	Ref.
$\text{Ba}_{0.98}\text{Ca}_{0.02}\text{Zr}_{0.02}\text{Ti}_{0.98}\text{O}_3$	---	1380 $^{\circ}\text{C}/3$ h	24	126	5305	1520	16.1	3.58	2.58	Present work
$\text{Ba}_{0.98}\text{Ca}_{0.02}\text{Zr}_{0.02}\text{Ti}_{0.98}\text{O}_3$	Cu	1380 $^{\circ}\text{C}/3$ h	22	126	4803	1434	14.2	3.34	2.49	Present work
$\text{Ba}_{0.98}\text{Ca}_{0.02}\text{Zr}_{0.02}\text{Ti}_{0.98}\text{O}_3$	Cu/Bi	1380 $^{\circ}\text{C}/3$ h	< 16	132	3377	1102	14	4.59	3.47	Present work
$\text{Ba}_{0.85}\text{Ca}_{0.15}\text{Ti}_{0.9}\text{Zr}_{0.1}\text{O}_3$	Cu/Y	1400 $^{\circ}\text{C}/4$ h	25	100	10175	4546	20	10.82	2.33	[18]
$\text{Ba}_{0.85}\text{Ca}_{0.15}\text{Ti}_{0.9}\text{Zr}_{0.1}\text{O}_3$	Bi	1350 $^{\circ}\text{C}/4$ h	20	94	~9200	3125	17	10.4	3.5	[21]
$\text{Ba}_{0.98}\text{Ca}_{0.02}\text{Zr}_{0.02}\text{Ti}_{0.98}\text{O}_3$	Cu	1250 $^{\circ}\text{C}/4$ h	25	120	~8500	~2000	20	11.6	3.7	[24]
$\text{Ba}_{0.98}\text{Ca}_{0.02}\text{Zr}_{0.02}\text{Ti}_{0.98}\text{O}_3$	Co	1400 $^{\circ}\text{C}/4$ h	22	107	~10000	2675	~20	11.5	3.1	[27]
$\text{Ba}_{0.98}\text{Ca}_{0.02}\text{Zr}_{0.02}\text{Ti}_{0.98}\text{O}_3$	Pr	1350 $^{\circ}\text{C}/2$ h	-	-	-	-	17.7	6.5	1.1	[28]
$\text{Ba}_{0.85}\text{Ca}_{0.15}\text{Ti}_{0.9}\text{Zr}_{0.1}\text{O}_3$	Cu/Nb	1400 $^{\circ}\text{C}/4$ h	-	75	20000	6056	23	12.6	0.25	[62]
$\text{Ba}_{0.85}\text{Ca}_{0.15}\text{Ti}_{0.9}\text{Zr}_{0.1}\text{O}_3$	Sr/Cu/Ta	1350 $^{\circ}\text{C}/4$ h	-	97	~11500	4569	19	13.39	-	[63]
$\text{Ba}_{0.98}\text{Ca}_{0.02}\text{Zr}_{0.05}\text{Ti}_{0.95}\text{O}_3$	Sr	1450 $^{\circ}\text{C}/2$ h	< RT	84	~6370	-	-	13.45	7.96	[64]
$\text{Ba}_{0.98}\text{Ca}_{0.02}\text{Zr}_{0.02}\text{Ti}_{0.98}\text{O}_3$	Mn	1400 $^{\circ}\text{C}/4$ h	~27	~120	~11000	1800	~19	15.7	1.8	[65]

4 Conclusions

The pure $\text{Ba}_{0.98}\text{Ca}_{0.02}\text{Zr}_{0.02}\text{Ti}_{0.98}\text{O}_3$ and Cu^{2+} , $\text{Cu}^{2+}/\text{Bi}^{3+}$ modified $\text{Ba}_{0.98}\text{Ca}_{0.02}\text{Zr}_{0.02}\text{Ti}_{0.98}\text{O}_3$ lead-free ceramics have been synthesised via solid-state reaction method and their structural, microstructural and electrical properties have been investigated systematically. The pure perovskite phase with a tetragonal structure has been revealed through XRD pattern, which further supports the results of dielectric measurements. The Nyquist plots from impedance spectroscopy indicate the contribution of grain and grain boundary in conduction. The main contribution of dopants reflected from the enhancement in temperature stability range and the observed optimum properties; T_{O-T} = below 16°C , $T_C = 132^\circ\text{C}$, $\epsilon_m \sim 4803$, $\tan\delta \sim 3.4\%$, $P_{\max} = 14 \mu\text{C}/\text{cm}^2$, $P_r = 4.59 \mu\text{C}/\text{cm}^2$ and $E_c = 3.47 \text{ kV}/\text{cm}$ for $\text{Cu}^{2+}/\text{Bi}^{3+}$ co-doped BCZT ceramics. Here, we have demonstrated that an appropriate amount of copper and bismuth can prove to be an effective way to further improve the temperature stability range, dielectric and ferroelectric properties to meet specific requirements for practical applications.

Acknowledgments

The authors express their sincere thanks to Prof. R.P. Chauhan, Physics Department, NIT-Kurukshetra for his kind support for SEM measurements. The authors also want to acknowledge the sincere efforts made by Mr. Vikas Narayan Thakur & Mr. Prashant Kumar, research scholars at CSIR-NPL, New-Delhi during ferroelectric and XRD measurements. Two of the authors, Amit Kumar and Sapna Kumari want to acknowledge the CSIR-New Delhi for providing financial support in the form of fellowship as SRF.

Author contributions

Sapna Kumari: Conceptualization, Methodology, Investigation, Data curation, Writing-original draft, Visualization. **Amit Kumar:** Methodology, Investigation, Data curation, Formal analysis. **V. Kumar:** Conceptualization, Investigation, Formal analysis, Visualization, Writing-original draft, Resources, Supervision, Writing - review & editing. **S. K. Dubey:** Methodology, Investigation, Formal analysis, Visualization, Writing - review & editing. **Parveen K. Goyal:** Conceptualization, Investigation, Formal analysis, Writing - review & editing. **Suresh Kumar:** Conceptualization, Investigation, Formal analysis, Resources. **A. L. Sharma:** Conceptualization, Methodology, Investigation, Resources, Writing-review & editing. **Anil Arya:** Methodology, Investigation, Formal analysis, Visualization, Writing - review & editing.

Conflict of interest: The authors declare that they have no conflict of interest.

References

1. B. Jaffe, W. R. Cook, H. Jaffe, *Piezoelectric Ceramics* (Academic Press, New York, 1971)
2. G.H. Haertling, *J. Am. Ceram. Soc.* 82, 797–818 (1999)
3. C.A. Randall, N. Kim, J-P. Kucera, W. Cao, T.R. Shrout, *J. Am. Ceram. Soc.* 81, 677–688 (1998)
4. T. Takenaka, H. Nagata, *J. Eur. Ceram. Soc.* 25, 2693–2700 (2005)
5. T.R. Shrout, S.J. Zhang, *J. Electroceramics* 19, 111–124 (2007)
6. Y. Saito, H. Takao, T. Tani, T. Nonoyama, K. Takatori, T. Homma, T. Nagaya, M. Nakamura, *Nature* 432, 84–87 (2004)
7. W. Liu, X. Ren, *Phys. Rev. Lett.* 103, 1–4 (2009)
8. J. Wu, D. Xiao, W. Wu, J. Zhu, J. Wang, *J. Alloys Compd.* 509, L359–L361 (2011)
9. A. Srinivas, R.V. Krishnaiah, V.L. Niranjani, S.V. Kamat, T. Karthik, S. Asthana, *Ceram. Int.* 41, 1980–1985 (2015)
10. Y. Zhang, H. Sun, W. Chen, *J. Phys. Chem. Solids* 114, 207–219 (2017)
11. M. Acosta, N. Novak, V. Rojas, S. Patel, R. Vaish, J. Koruza, G.A. Rossetti, J. Rödel, *Appl. Phys. Rev.* 4, 041305 (2017)
12. S.K. Ghosh, M. Ganguly, S.K. Rout, T.P. Sinha, *Eur. Phys. J. Plus*, (2015) DOI :10.1140/epjp/i2015-15068-6
13. W. Li, Z. Xu, R. Chu, P. Fu, G. Zang, *Mater. Lett.* 64, 2325–2327 (2010)
14. P. Wang, Y. Li, Y. Lu, *J. Eur. Ceram. Soc.* 31, 2005–2012 (2011)
15. J. Li, X. Sun, X.S. Zhang, Q. Chen, Z.H. Peng, P. Yu, *Phys. Status Solidi A* 210 N(3), 533–537 (2013)
16. T. Chen, T. Zhang, G. Wang, J. Zhou, J. Zhang, Y. Liu, *J. Mater. Sci.* 47, 4612–4619 (2012)
17. C.F. Yang, L. Wu, T.S. Wu, *J. Mater. Sci.* 27, 6573–6578 (1992)
18. Y. Wu, F. Ma, J. Qu, Y. Luo, J. Song, G. Wei, Y. Zhang, T. Qi, *Ceram. Int.* 44, 15001–15009 (2018)
19. H.X. Li, X.D. Jian, X. Niu, Y.B. Yao, T. Tao, B. Liang, S.G. Lu, *Scr. Mater.* 176, 67–72 (2020)
20. X. Wang, P. Liang, L. Wei, X. Chao, Z. Yang, *J. Mater. Sci.: Mater. Electron.* 27, 3217–3226 (2016)
21. R. Hayati, M.A. Bahrevar, T. Ebadzadeh, V. Rojas, N. Novak, J. Koruza, *J. Eur. Ceram. Soc.* 36, 3391–3400 (2016)
22. S. Zhou, Q. Liu, P. Xu, L. Yao, E. Cai, *Ferroelectrics* 510, 27–33 (2017)
23. J. Wu, D. Xiao, W. Wu, Q. Chen, J. Zhu, Z. Yang, J. Wang, *Scr. Mater.* 65, 771–774 (2011)
24. H. Sun, Y. Zhang, X. Liu, Y. Liu, W. Chen, *Ceram. Int.* 41, 555–565 (2015)
25. A. Nahar, M.A. Bhuiyan, M.J. Rahman, S. Choudhury, *Biointerface Res. Appl. Chem.* Volume 11(3), 9862–9870 (2021)
26. N. Kumada, H. Ogiso, K. Shiroki, S. Wada, Y. Yonesaki, T. Takei, N. Kinomura, *Mater. Lett.* 64, 383–385 (2010)
27. H. Sun, Y. Zhang, X. Liu, Y. Liu, S. Guo, W. Chen, *J. Mater. Sci.: Mater. Electron.* 25, 3962–3966 (2014)

28. Ramovatar, I. Coondoo, S. Satapathy, N. Panwar, *Ceram. Int.* 44, 1690–1698 (2017)
29. Y. Zhang, H.J. Sun, W. Chen, *J. Alloys Compd.* 694, 745–751 (2017)
30. X. Chen, X. Ruan, K. Zhao, X. He, J. Zeng, Y. Li, L. Zheng, C.H. Park, G. Li, *J. Alloys Compd.* 632, 103–109 (2015)
31. J.P. Praveen, V.R. Monaji, E. Chandrakala, S. Indla, S.D. kumar, V. Subramanian, D. Das, *J. Alloys Compd.* 750, 392–400 (2018)
32. S. Mahajan, O.P. Thakur, D.K. Bhattacharya, K. Sreenivas, *J. Phys. D: Appl. Phys.* 42, 065413 (2009)
33. X. Wang, P. Liang, Z. Yang, *J. Ceram. Soc. JAPAN* 126 (6), 440–446 (2018)
34. X. Kuang, G. Carotenuto, L. Nicolais, *Adv. Perform. Mater.* 4, 257–274 (1997)
35. M. Arshad, D. Huiling, J. M. Sufyan, A. Maqsood, I. Ashraf, S. Hussain, W. Ma, H. Ran, *Ceram. Int.* 46, 2238–2246 (2019)
36. B. D. Cullity, S. R. Stock, *Elements of X-Ray Diffraction* (Third Edition, Pearson, 2014)
37. J. Rodrigues-Carvajal, FULLPROF A Rietveld refinement and pattern matching analysis program, laboratoire leon Brillouin (CEA-CNRS), France, (2000)
38. S. Carbonin, Martignago, F., Menegazzo, G., Negro, A.: *Phys. Chem. Miner.* 29, 503–514 (2002)
39. S. Yotthuan, T. Bongkarn, *Int. J. Sci.* 14(2), 33–42 (2017)
40. N. Liu, R. Liang, Z. Zhou, X. Dong, *X. J. Mater. Chem. C* 6, 10211–10217 (2018)
41. S. Butee, K.R. Kambale, A. Ghorpade, A. Halikar, R. Gaikwad, H. Panda, *J. Asian Ceram. Soc.* 7(4), 407–416 (2019)
42. S. Guo, B. Luo, H. Xing, J. Wang, H. M. Zeeshan, K. Jin, C. Chen, *Ceram. Int.* 46, 7198–7203 (2019)
43. S. Sharma , H. Sharma, S. Kumar, S. Thakur, R.K. Kotnala, N. S. Negi, *J. Mater. Sci.: Mater. Electron* 31, 19168–19179 (2020)
44. Z. Hanani, D. Mezzane, M. Amjoud, S. Fourcade, A.G. Razumnaya, I.A. Luk'yanchuk, M. Gouné, *Superlattices Microstruct* 127, 109 (2019)
45. Q. Zhang, J. Chen, M. Che, *Ferroelectrics* 566, 30–41 (2020)
46. G. Yao, X. Wang, Y. Yang, L. Li, *J. Am. Ceram. Soc.* 93 (6), 1697–1701 (2010)
47. V.N. Thakur, A. Zafer, S. Yadav, A. Kumar, *Sensors and Actuators A* 297, 111536 (2019)
48. X. Ji, C. Wang, S. Zhang, R. Tu, Q. Shen, J. Shi, L. Zhang, *J. Mater. Sci.: Mater. Electron.* 30, 12197–12203 (2019)
49. V.S. Vinila, J.K. Isac, *International Journal of Science and Research (IJSR)* 7, 696-703 (2018)
50. V.N. Thakur, S. Yadav, A. Kumar, (2020)
<https://doi.org/10.1016/j.mtcomm.2020.101846>
51. X. Chen, X. Li, H. Zhou, J. Sun, X. Li, X. Yan, C. Sun, J. Shi, *J. Adv. Ceram.* 8(3), 427–437 (2019)
52. L. Wang, W. Bai, X. Zhao, F. Wen, L. Li, W. Wu, P. Zheng, J. Zhai, *J. Mater. Sci.: Mater. Electron.* 30, 9219–9230 (2019)
53. S. Sapparjya, T. Badapanda, S. Behera, B. Behera & Piyush R. Das, *Phase Transit.* 93, 245–262 (2020)
54. Z. Wang, X. Chen, X. Chao, J. Wang, P. Liang, Z. Yang, *Ceram. Int.* 42, 18037–18044 (2016)

55. X.W. Wang, B.H. Zhang, Y.Y. Li, Y.C. Shi, L.Y. Sun, G. Feng, C.L. Li, Y.F. Liang, Y.P. Zheng, S.Y. Shang, J. Shang, Y.C. Hu, S.Q. Yin, *J. Mater. Sci.: Mater. Electron.* 31, 4732–4742(2020)
56. Y. Zhang, M. Xie, J. Roscow, Y. Bao, K. Zhou, D. Zhang, C.R. Bowen, *J. Mater. Chem. A* 5, 6569–6580 (2017)
57. C. Padurariu, L. Padurariu, L. Curecheriu, C. Ciomaga, N. Horchidan, C. Galassi, L. Mitoseriu, *Ceram. Int.* 43, 5767–5773 (2017).
58. Z. Hanani, S. Merselmiz, D. Mezzane, M. Amjoud, A. Bradesko, B. Rozic, M. Lahcini, M.E. Marssi, A.V. Ragulya, I.A. Lukyanchuk, Z. Kutnjak, M. Goune, *RSC Adv.* 10, 30746 (2020)
59. Y. Huang, F. Li, H. Hao, F. Xia, H. Liu, S. Zhang, *J. Materiomics* 5, 385–393 (2019)
60. A.P. Sharma, D.K. Pradhan, S.K. Pradhan, M. Bahoura, *Sci. Rep.* 9, 16809 (2019)
61. W. Cai, Y. Fan, J. Gao, C. Fu, X. Deng, *J. Mater. Sci. Mater. Electron.* 22, 265 (2011)
62. H. Zhao, W. Ma, J. Guo, X. Zang, P. Miao, M. Ma, F. Zhang, *J. Mater. Sci.: Mater. Electron.* 29, 2949–2957 (2017)
63. Y. Wu, X. Liu, Q. Zhang, M. Jiang, Y. Liu, X. Liu, *J. Mater. Sci.: Mater. Electron.* 24, 5199–5203 (2013)
64. P.K. Roy, B. Ponraj, K.B.R. Varma, *Ceram. Int.* 43, 15762–15768 (2017)
65. H. Sun, S. Duan, X. Liu, D. Wang, H. Sui, *J. Alloys Compd.* 670, 262–267 (2016)

Figures

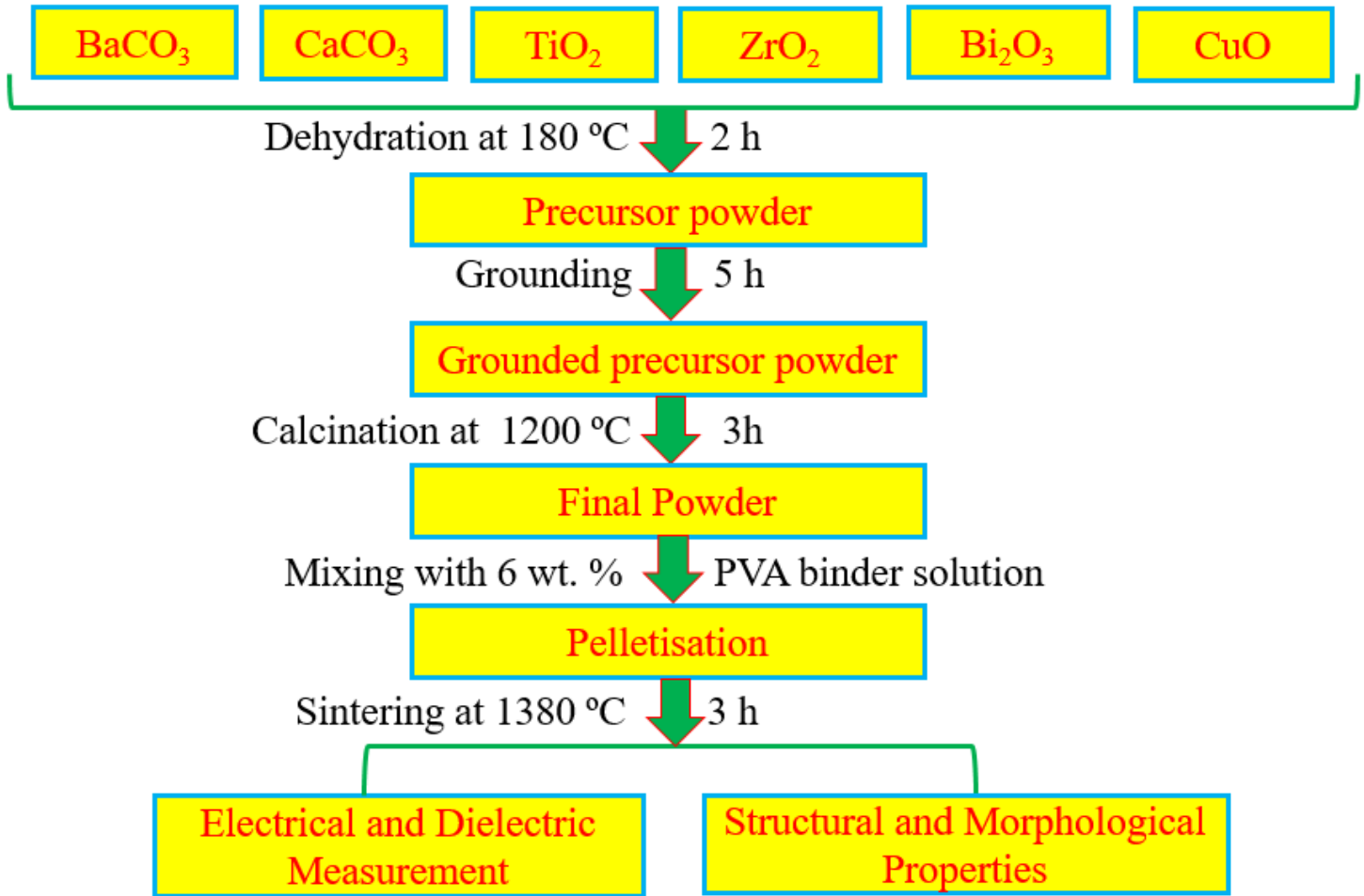


Figure 1

The schematic diagram showing the different steps of solid-state reaction method followed for the synthesis of BCZT based ceramic samples.

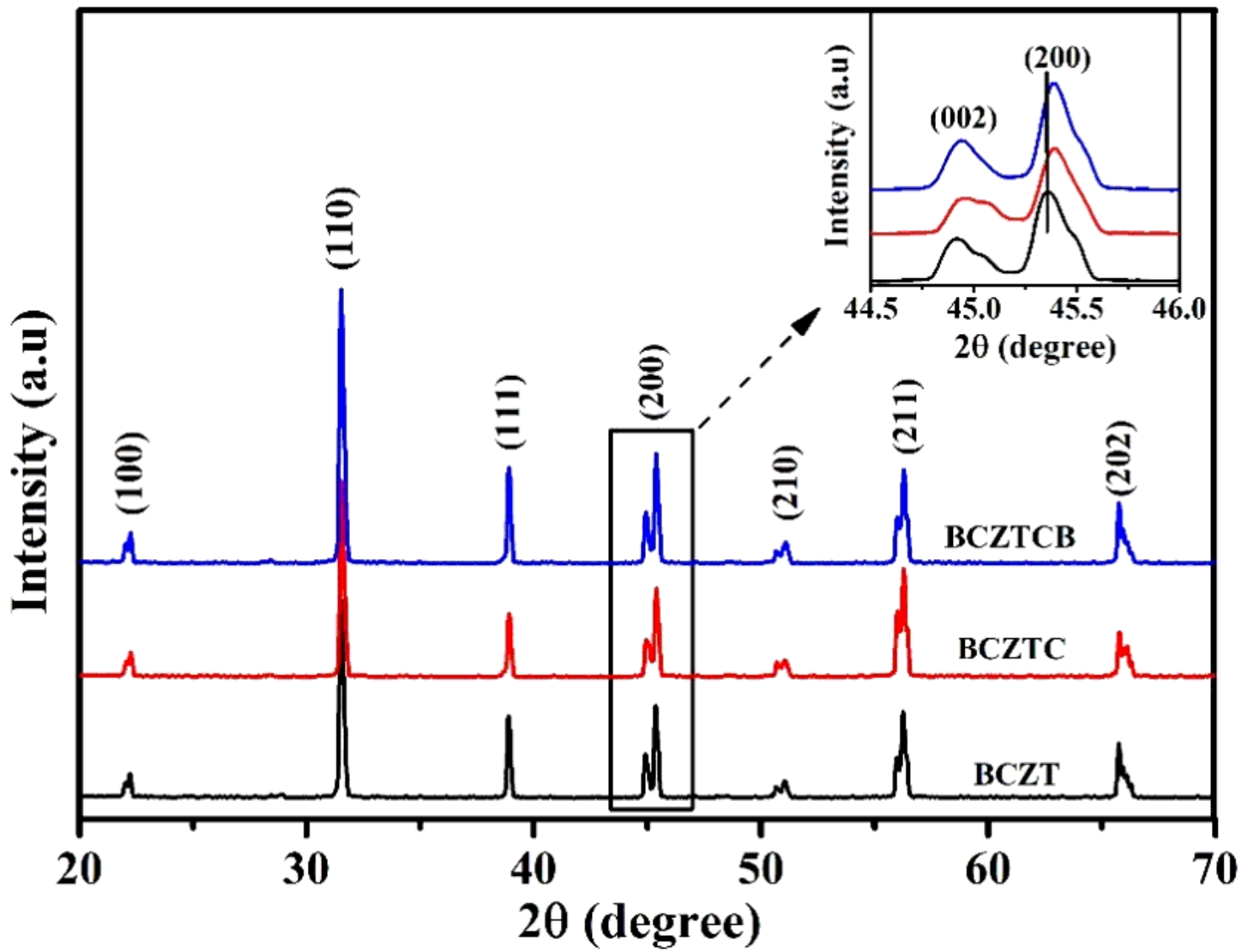


Figure 2

XRD patterns of sintered BCZT, BCZTC and BCZTCB ceramic samples (inset shows the enlarged region for $2\theta = 44.5^\circ - 46^\circ$).

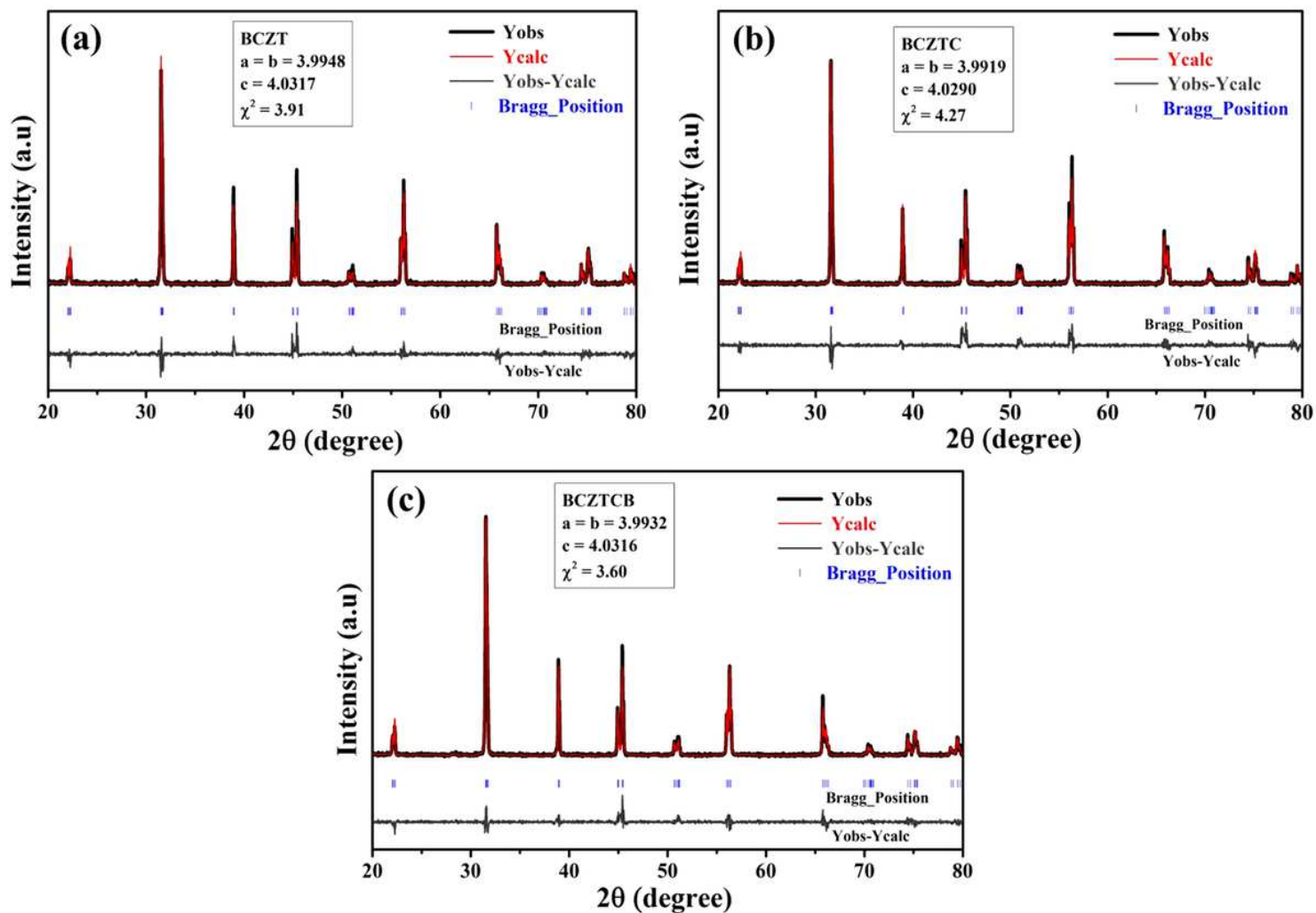


Figure 3

Rietveld refinement fitting for (a) BCZT, (b) BCZTC and (c) BCZTCB ceramic samples.

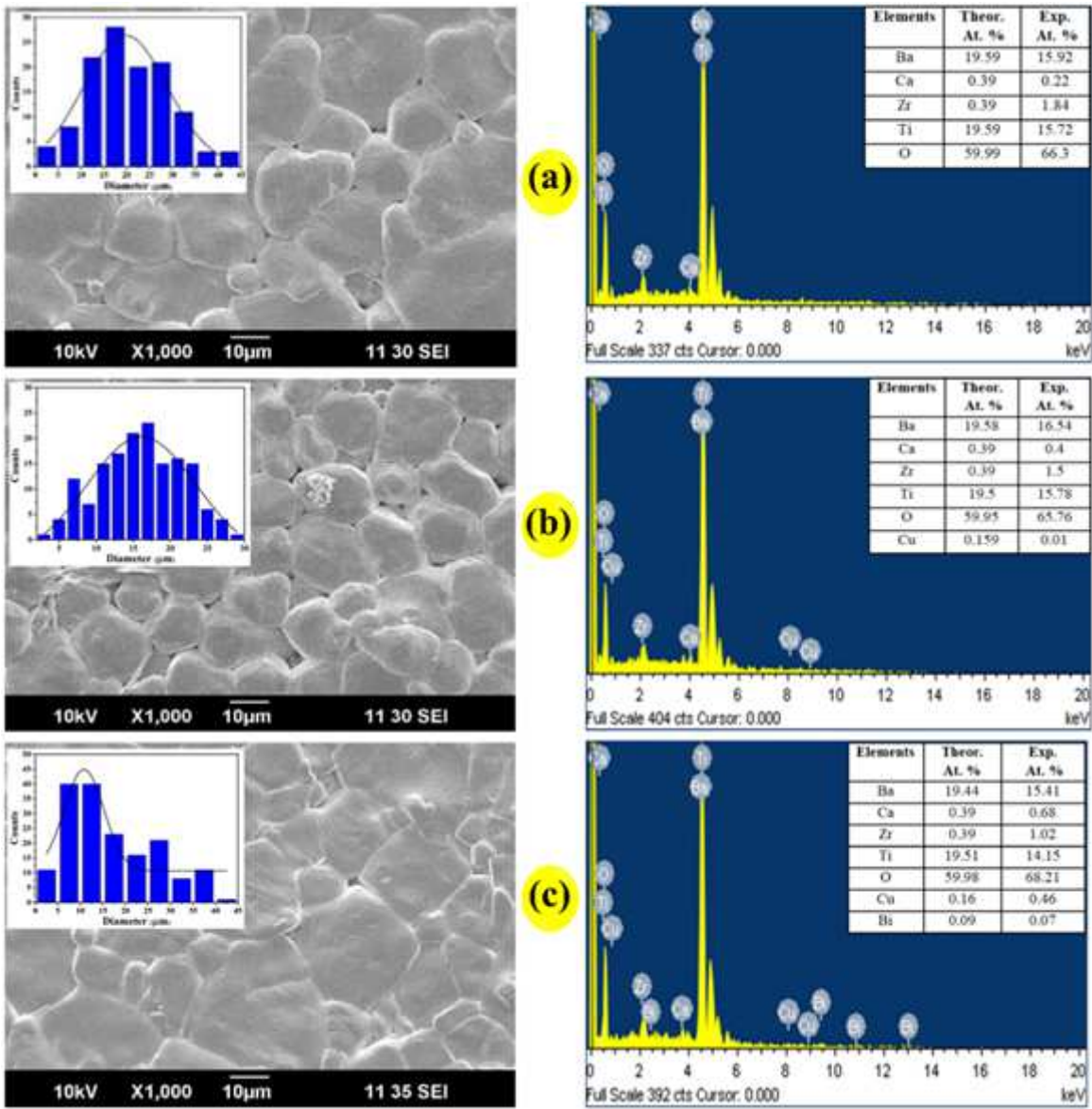


Figure 4

SEM images and EDX spectra of (a) BCZT (b) BCZTC (c) BCZTCB ceramic samples (Inset: grain size distribution and Comparison of atomic % detected by EDX).

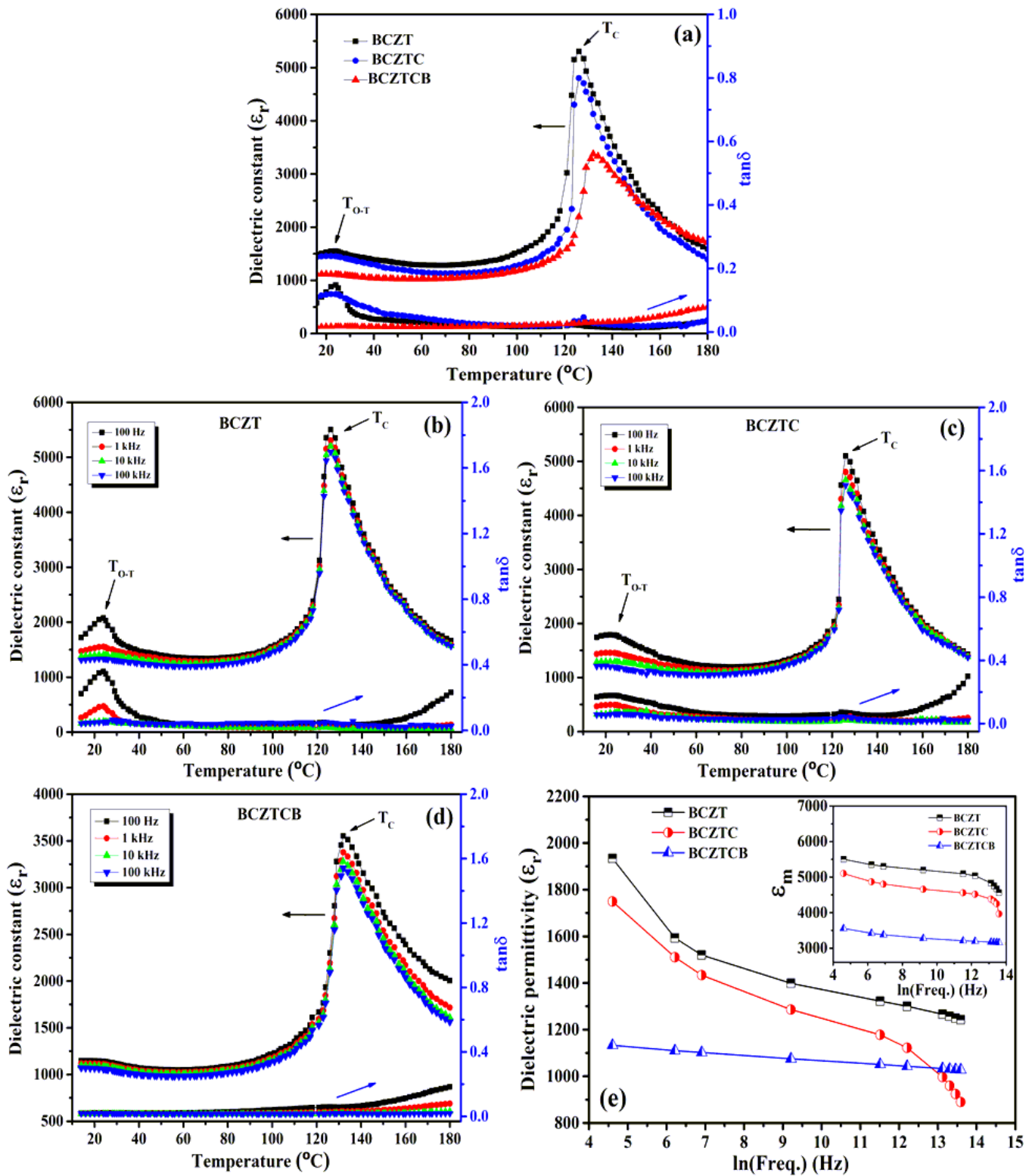


Figure 5

Temperature dependence of dielectric permittivity and loss (a) at 1 kHz, (b-d) at different frequencies (e) frequency dependence of room temperature dielectric permittivity (Inset shows maximum dielectric permittivity vs. frequency).

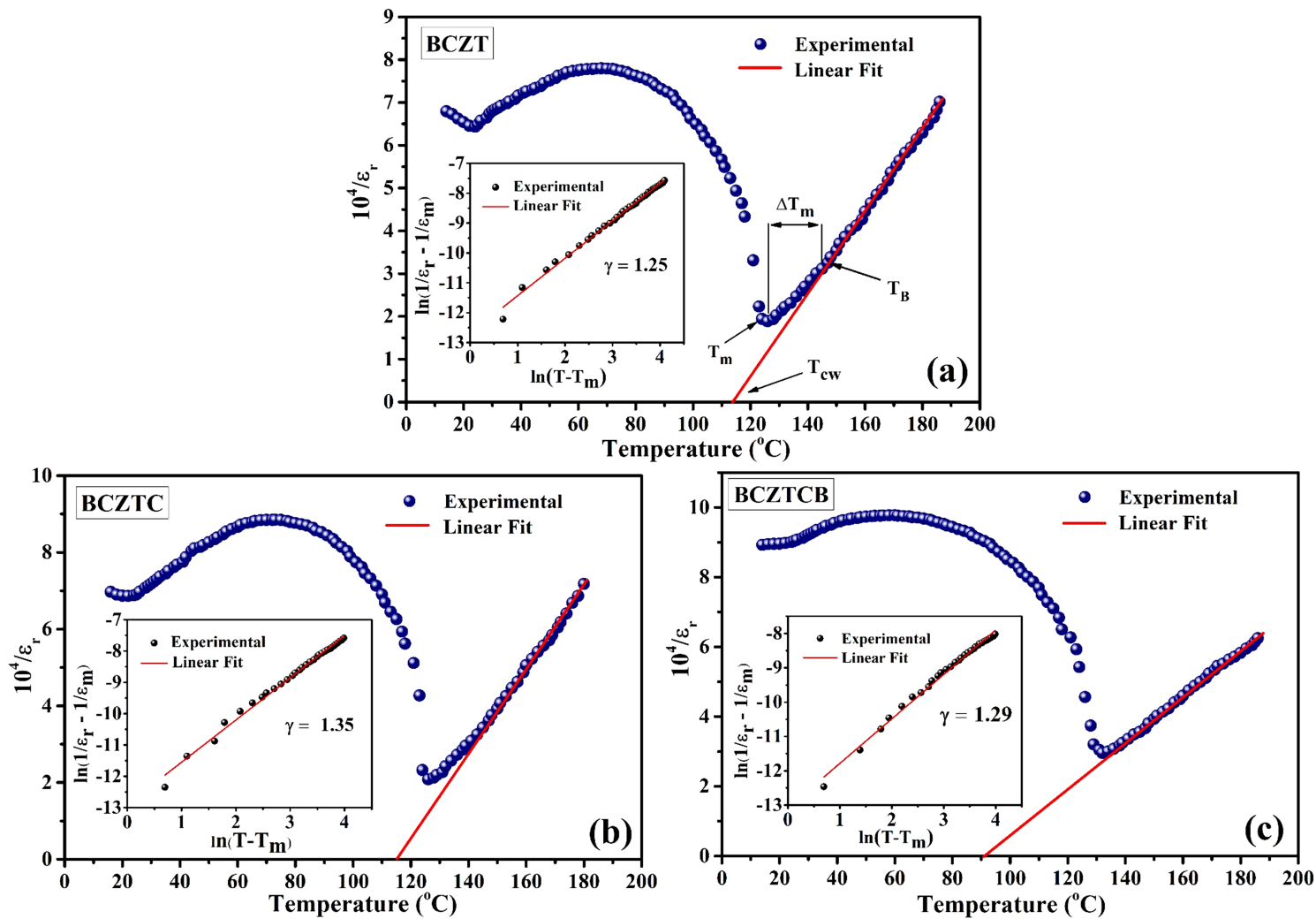


Figure 6

Temperature dependence of inverse dielectric constant (a) BCZT, (b) BCZTC, (c) BCZTCB and Insets; Plot of $\ln(1/\epsilon_r - 1/\epsilon_m)$ vs. $\ln(T - T_m)$ at 1 kHz.

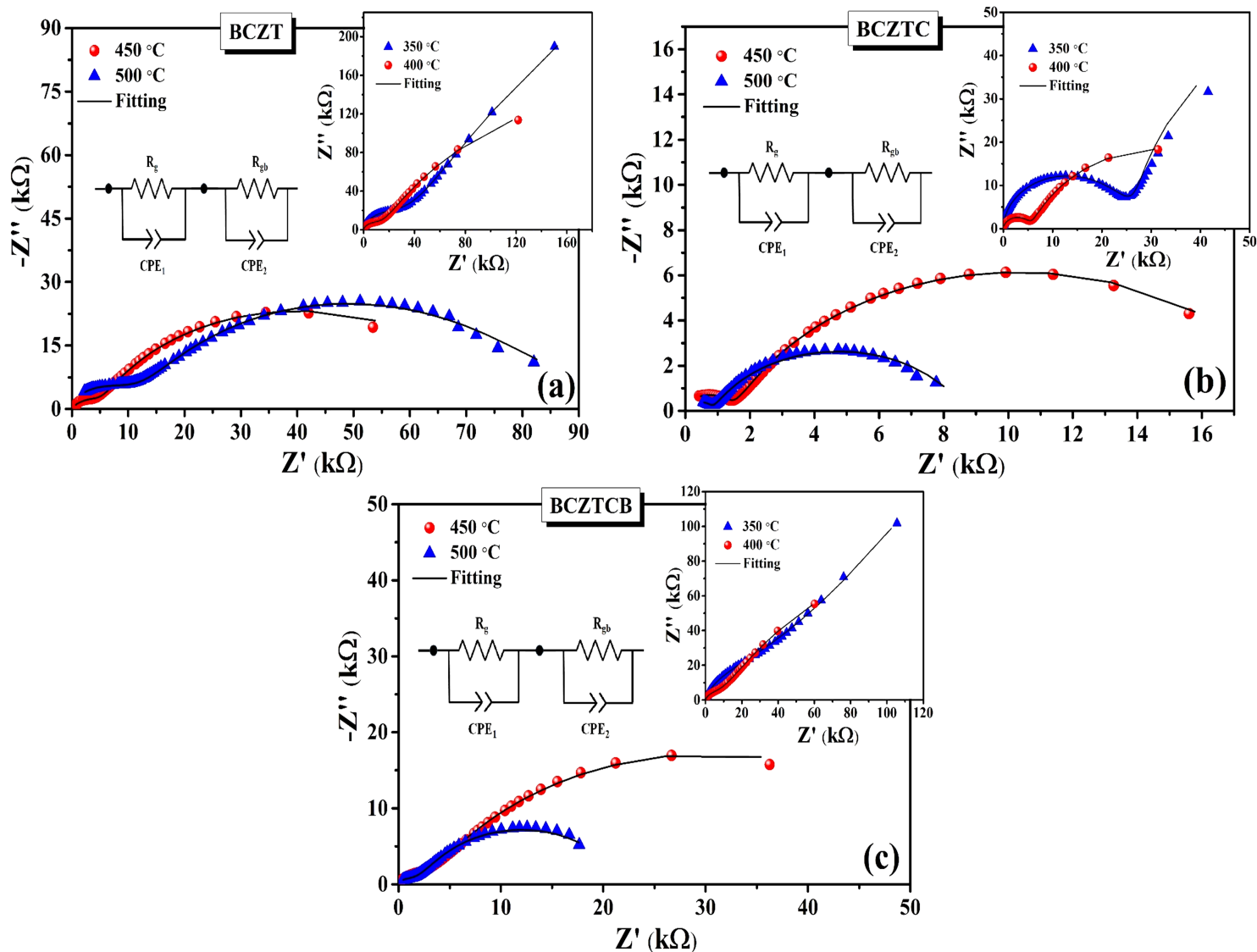


Figure 7

Nyquist plots of (a) BCZT, (b) BCZTC and (c) BCZTCB eramics at temperatures (450 C° & 500 °C). Insets: Nyquist plots of (a) BCZT, (b) BCZTC and (c) BCZTCB at temperatures (350 C° & 400 °C).

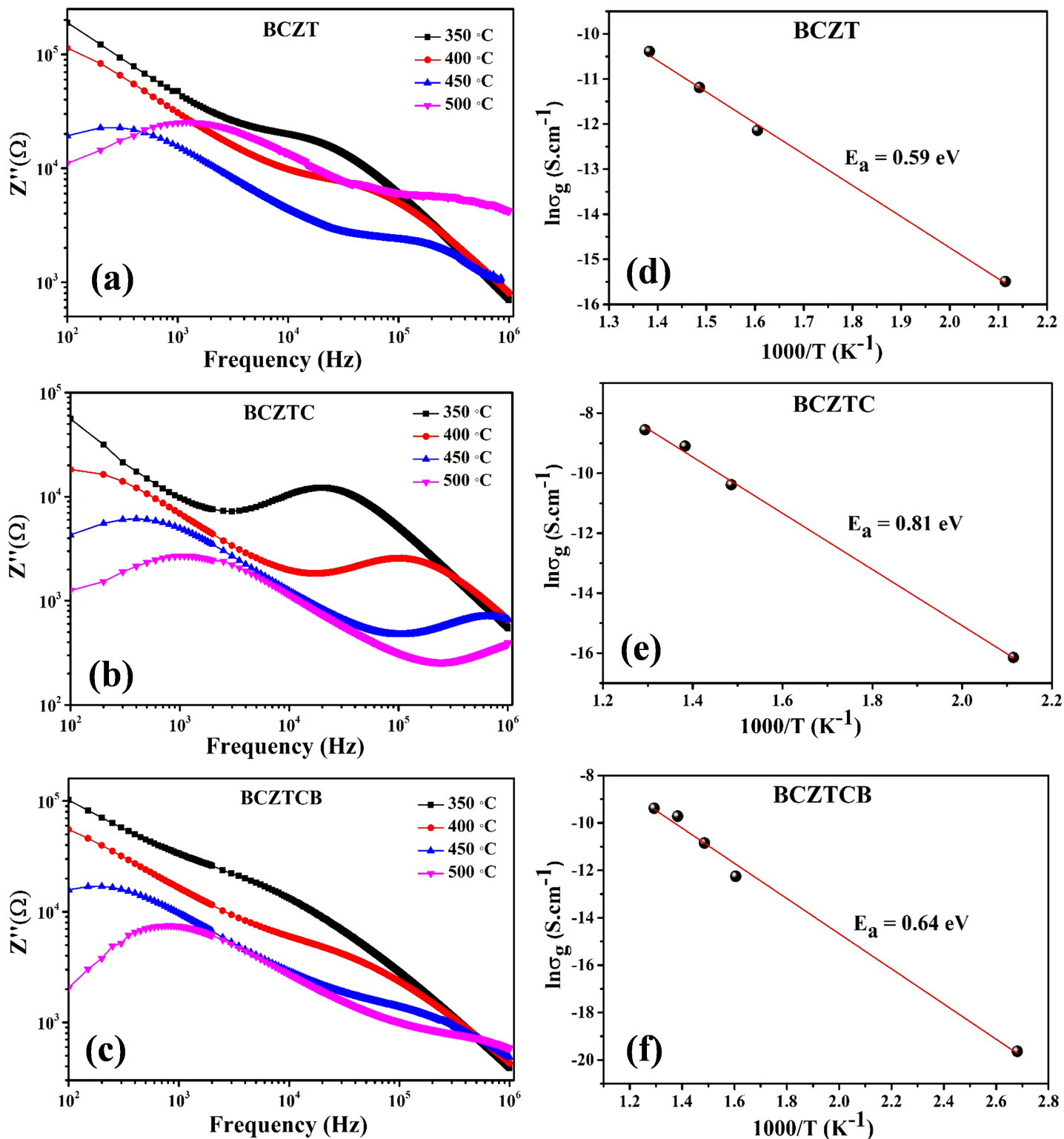


Figure 8

Frequency dependent imaginary part of impedance at different temperatures, (a) BCZT, (b) BCZTC, and (c) BCZCB. (d-f) plots of $\ln(\sigma_g)$ vs $1000/T$ for BCZT, BCZTC, and BCZCB respectively.

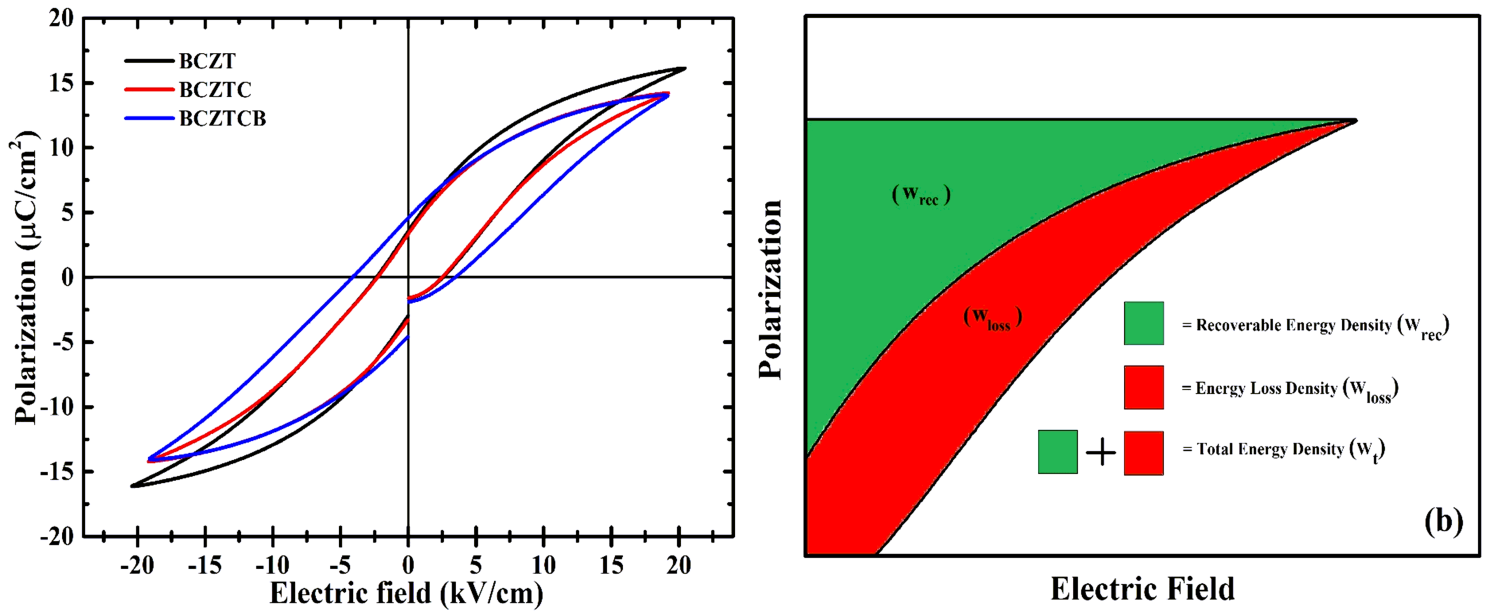


Figure 9

(a) P-E Hysteresis loop at 10 Hz for BCZT, BCZTC and BCZTCB ceramics (b) schematic representation of the areas representing the recoverable energy density, Energy loss density and total energy.